

# PGVMS: A Prompt-Guided Unified Framework for Virtual Multiplex IHC Staining with Pathological Semantic Learning

Fuqiang Chen, Ranran Zhang, Wanming Hu, Deboch Eyob Abera, Yue Peng, Boyun Zheng, Yiwen Sun, Jing Cai and Wenjian Qin

**Abstract**—Immunohistochemical (IHC) staining enables precise molecular profiling of protein expression, with over 200 clinically available antibody-based tests in modern pathology. However, comprehensive IHC analysis is frequently limited by insufficient tissue quantities in small biopsies. Therefore, virtual multiplex staining emerges as an innovative solution to digitally transform H&E images into multiple IHC representations, yet current methods still face three critical challenges: (1) inadequate semantic guidance for multi-staining, (2) inconsistent distribution of immunochemistry staining, and (3) spatial misalignment across different stain modalities. To overcome these limitations, we present a prompt-guided framework for virtual multiplex IHC staining using only uniplex training data (PGVMS). Our framework introduces three key innovations corresponding to each challenge: First, an adaptive prompt guidance mechanism employing a pathological visual language model dynamically adjusts staining prompts to resolve semantic guidance limitations (Challenge 1). Second, our protein-aware learning strategy (PALS) maintains precise protein expression patterns by direct quantification and constraint of protein distributions (Challenge 2). Third, the prototype-consistent learning strategy (PCLS) establishes cross-image semantic interaction to correct spatial misalignments (Challenge 3). Evaluated on two benchmark datasets, PGVMS demonstrates superior performance in pathological consistency. In general, PGVMS represents a paradigm shift from dedicated single-task models toward unified virtual staining systems.

**Index Terms**—Prompt guidance, Multiplex staining, Semantic preserving, Virtual stain

This work was supported in part by the Ministry of Science and Technology's key research and development program (2023YFF0723400), National Natural Science Foundation of China (No. 62271475), Shenzhen-Hong Kong Joint Lab on Intelligence Computational Analysis for Tumor Imaging (E3G111), Guangdong Youth Talent program (2024TQ08A386), and the Youth Innovation Promotion Association CAS (2022365). (Fuqiang Chen and Ranran Zhang contributed equally to this work.) (Corresponding author: Wenjian Qin.)

Fuqiang Chen, Deboch Eyob Abera and Yue Peng are with the Shenzhen Institutes of Advanced Technology, Chinese Academy of Sciences and University of Chinese Academy of Sciences, Beijing, China.

Wanming Hu is with the Department of Pathology, Sun Yat-sen University Cancer Center, State Key Laboratory of Oncology in South China, Guangzhou, China.

Jing Cai and Yiwen Sun are with the Hong Kong Polytechnic University, Hong Kong SAR, China (e-mail: jing.cai@polyu.edu.hk).

Boyun Zheng is with the Department of Electronic Engineering, The Chinese University of Hong Kong, Hong Kong SAR 999077, China

Wenjian Qin and Ranran Zhang are with the Shenzhen Institutes of Advanced Technology, Chinese Academy of Sciences, Shenzhen, China (e-mail: wj.qin@siat.ac.cn).

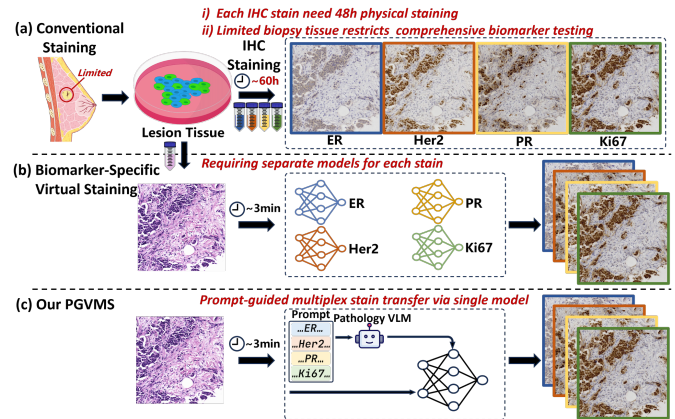
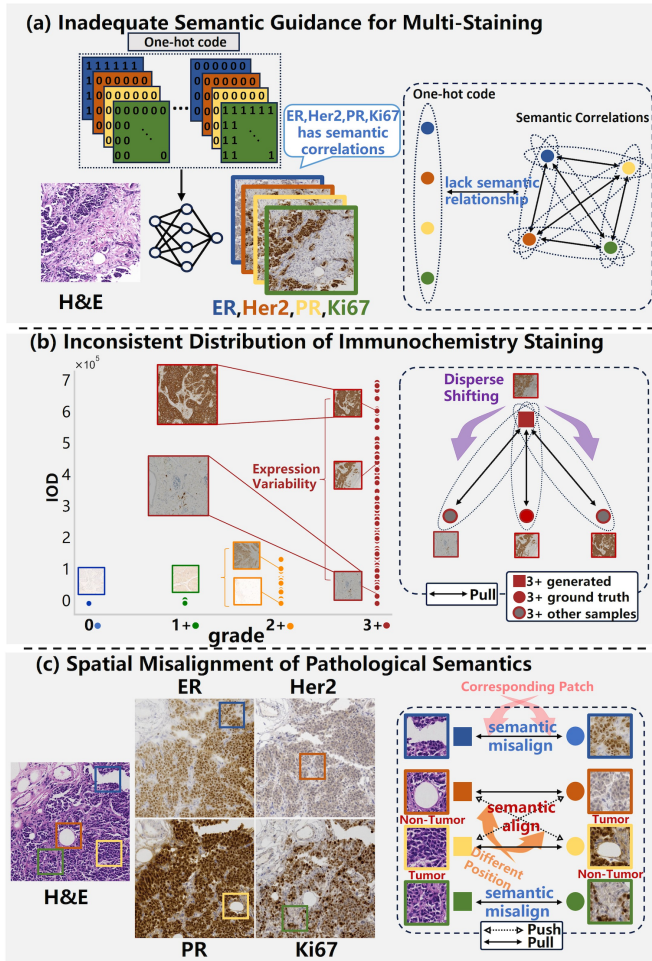


Fig. 1: The comparison of traditional IHC staining and virtual staining workflows. From (a) to (c), they are conventional IHC staining, biomarker-specific virtual staining and our PGVMS.

## I. INTRODUCTION

CANCER diagnosis primarily depends on histopathological analysis, with hematoxylin and eosin (H&E) staining remaining the gold standard by providing exceptional visualization of tissue morphology through its characteristic nuclear (blue/purple) and cytoplasmic (pink) differentiation [1]. While H&E staining offers excellent morphological assessment, molecular biomarker identification requires more advanced techniques such as multiplex immunohistochemistry (mIHC), which enables simultaneous detection of multiple critical biomarkers within a single tissue section [2]. However, mIHC analysis faces dual practical limitations: (1) insufficient tissue quantities in small biopsies constrain comprehensive biomarker assessment, and (2) specialized equipment and time-consuming protocols (up to 60 hours [3]) restricts its availability in resource-limited settings (Fig. 1a).

Virtual staining has emerged as a promising computational approach for pathological analysis, as illustrated in Fig. 1b. This AI-based technique enables digital transformation of H&E-stained images into IHC representations, simulating biomarker expression patterns without physical staining. However, biomarker-specific virtual staining methods face inefficiency and inconsistency issues, as they require separate models for each stain.



**Fig. 2:** Three challenges of virtual multi-staining. (a) Inadequate semantic guidance for multi-staining. (b) Inconsistent distribution of immunohistochemistry staining. (c) Spatial misalignment of pathological semantics.

The field of virtual staining has evolved through three stages: (1) initial GAN-based implementations lacking pathological constraints [4]–[6], (2) subsequently, intermediate solutions incorporating hierarchical semantic information at progressively finer scales (grade-level [7], patch-level [8]–[10]), and (3) some solutions achieving pixel-level precision [11]–[13]. Significantly, recent breakthroughs enable controlled multi-marker generation through various approaches: Guan et al. [14] developed multi-stain using a shared encoder with four dedicated decoders to exploit inter-marker correlations, while other methods employ one-hot encoding for discrete biomarker selection [15] or CLIP-based text embedding for prompt control [16].

Rethinking the existing methods and challenges of virtual multiplex staining in H&E to IHC, three significant challenges emerge (Fig. 2): **(a) Inadequate semantic guidance for multi-staining:** Existing virtual multi-staining methods primarily employ one-hot encoding, which artificially enforces categorical independence among molecular markers while disregarding their inherent biological correlations in tissue expression. Although CLIP-based prompt guidance has

been proposed to mitigate this limitation, its general-domain pretraining lacks pathology-specific adaptation, resulting in imprecise histopathological semantic capture. Consequently, current frameworks cannot effectively achieve semantic-aware co-staining generation for multiple biomarkers. **(b) Inconsistent distribution of immunohistochemistry staining:** Current approaches fail to adequately capture fine-grained molecular semantics in pathological images, particularly the precise protein expression levels within specific stained regions. This limitation is especially evident in 3+ grade whole slide images (WSIs), where significant intra-grade variation in protein expression levels exists. By relying solely on coarse grade-level annotations rather than quantifying actual protein expression, existing methods disperse critical molecular-level pathological information, resulting in inconsistent immunohistochemistry staining distributions between generated and ground-truth IHC images. **(c) Spatial misalignment of pathological semantics:** Typically, virtual staining GT pairs are obtained from two depth-wise consecutive cuts of the same tissue, which are then stained separately. This approach inevitably prevents pixel-perfect image correspondences due to changes in cell morphology and staining-induced degradation. Inherent spatial inconsistencies exist between input images (H&E) and label images (IHC), meaning that corresponding patches in paired images may contain different normal and tumor cells. Representations with similar semantics may be incorrectly separated and those with opposing semantics may be incorrectly merged. This affects the training efficiency of the model and the semantic accuracy of the generated images.

To address the aforementioned challenges, we propose a novel prompt-guided framework for virtual multiplex IHC staining (PGVMS). PGVMS advances virtual multiplex staining by incorporating semantic-preserving mechanisms to maintain critical pathological relationships across different staining modalities. We introduce one novel generator and two innovative learning strategies to tackle the corresponding problems: (a) For inadequate semantic guidance on multi-stain generation, we propose a pathological semantics-style guided (PSSG) generator that leverages the CONCH pathology visual language model for prompt-guided stain generation. This approach enables efficient virtual multi-staining by incorporating rich semantic embeddings, ensuring accurate and context-aware transformations from H&E to multiple IHC stains, such as ER, PR, HER2, and Ki67. (b) For inconsistent distribution of immunohistochemistry staining, we directly quantify the protein expression in each IHC-stained image by calculating the optical density in the DAB channel [3]. This approach preserves molecular-level pathological semantics. Additionally, we propose a novel focal optical density (FOD) map that adaptively re-weights contributions from protein-expressing regions and normal tissue during quantification, providing a more accurate and robust representation of protein expression levels. (c) For spatial misalignment of pathological semantics, we assume that the pathological content of the generated image align with the label. To enhance pathological semantic interaction despite spatial inconsistencies, we facilitate the convergence of pathological features towards cross-corresponding prototypes in both the generated image and the label. This ensures

semantic consistency even in the presence of spatial variations.

The main contributions of this paper are as follows:

- We develop a pathological semantics–style guided (PSSG) generator by integrating a pathology visual language model, enabling prompt-driven semantic embedding for biologically informed multiplex IHC generation.
- To preserve molecular-level pathological semantics, a protein-aware learning strategy (PALS) is introduced to explicitly quantify and constrain protein expression distributions via optical density modeling.
- We further propose a prototype-consistent learning strategy (PCLS) to align high-protein expression prototypes with the label, effectively addressing spatial misalignment.
- Comprehensive experiments on the MIST, IHC4BC, and cross-organ clinical datasets demonstrate that the proposed method achieves state-of-the-art virtual staining accuracy while enabling efficient multiplex IHC generation.

## II. RELATED WORKS

### A. Image-to-Image Translation

Image-to-image translation (I2I) aims to transform an input image from a source domain to a target domain while preserving content and transferring style. Early methods like pix2pix [4] and CycleGAN [6] used conditional GANs and cyclic consistency for supervised and unpaired translation, respectively. Park *et al.* [5] introduced Contrastive Unpaired Translation (CUT), which leverages contrastive learning in a patch-based manner to maximize mutual information between input-output pairs. However, some argue that traditional I2I methods often fail to capture domain-specific details and are limited to one-to-one mappings. For example, Kazemi *et al.* [17] extended CycleGAN to enable one-to-many mappings by learning domain-specific codes, while Almahairi *et al.* [18] proposed augmented CycleGAN for many-to-many multimodal translations. These advancements, with CUT as a key innovation, highlight the importance of balancing content preservation, style transfer, and output diversity in I2I tasks. But these methods are constrained in direct application due to their inability to explicitly preserve pathological semantics. In recent years, diffusion-based I2I frameworks have emerged as powerful alternatives, offering stronger generative priors and controllable synthesis. For instance, ControlNet [19] introduces conditional control structures to guide diffusion models with external cues such as edges or segmentation maps, enabling fine-grained structural preservation. UNSB (Unpaired Noise Scheduling Bridge) [20] formulates I2I as a noise-bridging process between source and target domains, improving domain adaptation and stability. DDBM (Denosing Diffusion Bridge Model) [21] further extends this concept by explicitly learning domain-conditioned diffusion paths, facilitating faithful translation while maintaining semantic consistency. These diffusion-based paradigms significantly enhance fidelity and controllability, marking a new era for I2I applications, including virtual staining.

### B. Virtual Staining

Virtual staining using GANs has advanced significantly in recent years. Existing methods focus on extracting pathological semantic information from inconsistent ground truth pairs. For example, Liu *et al.* [8] proposed PyramidP2P, a pyramid pix2pix image generation method, but it requires pixel-level paired data, which is hard to obtain. At the image level, Zeng *et al.* [7] ensured virtual IHC accuracy with a Pos/Neg classifier. At the patch level, Li *et al.* [10] introduced ASP, which uses patch-based contrastive learning to tolerate partial data misalignment. At the pixel level, Liu *et al.* [11] transformed H&E to Ki67 using a pathology representation network with expert-annotated labels. Peng *et al.* [12] extracted tumor information from labeled images using a nuclear density detector to align tumor locations. However, these methods struggle with severe spatial misalignment. To address this, Chen *et al.* [13] proposed PSPStain, which detects tumor protein expression in patches and uses prototype learning for cross-spatial semantic alignment. For virtual multiplex staining, Lin *et al.* [15] used style-guided normalization with one-hot encoding to transform one staining type into multiple types. Xiong *et al.* [22] optimizes visual prompts to control content and style. Zhang *et al.* [9] disentangled style and content to generate multiple staining types while predicting positive signals. Guan *et al.* [14] developed Multi-IHC, using a shared encoder and four decoders. Dubey *et al.* [16] introduced VIMs, leveraging CLIP [23] for prompt embeddings (e.g., “CDX2”) and fine-tuning a diffusion model with LoRA for prompt-controlled multi-virtual staining.

Despite their potential, current virtual multiplex staining methods face notable limitations. One-hot encoding approaches [15] treat molecular markers as independent categories, ignoring biological correlations and limiting semantic richness. Prompt-guided methods, such as Dubey *et al.* [16], employ CLIP embeddings with LoRA-finetuned diffusion models for prompt-controlled multiplex staining. However, CLIP is pretrained on general-domain text-image data rather than pathology-specific pairs, so it fails to capture the semantic relationships among different IHC stains. Other methods, such as Zhang *et al.* [9], cannot control which stain is generated individually, producing multiple stains simultaneously. Additional approaches [7], [8], [10]–[14] rely on biomarker-specific models, which are computationally inefficient and do not scale well for multiple stains. These limitations motivate the need for pathology-aware semantic guidance mechanisms to achieve efficient and biologically consistent multiplex virtual staining.

### C. Pathological Visual Language Model

In recent years, the development of pathological visual language models (VLMs) has significantly advanced computational pathology, enabling more accurate and efficient analysis of histopathological images. Among these models, MUSK [24], PLIP [25], and CONCH [26] stand out as notable contributions. MUSK, a vision-language foundation model for precision oncology, achieves state-of-the-art performance by employing a two-stage training paradigm: first, masked learning on 50 million tissue patches and 1 billion textual

tokens, followed by contrastive learning on 1 million image-text pairs. PLIP, on the other hand, utilizes a dataset of over 200,000 pathology image-text pairs sourced from medical Twitter, which enables PLIP to perform tasks like zero-shot classification and cross-modal retrieval. CONCH [26] focus on IHC image-text pairs, trained on 1.17 million pathology image-caption pairs. It excels in generating representations for non-H&E stains, such as IHC and special stains, capturing nuanced relationships between images and text. These models significantly advance computational pathology through large-scale data and multi-modal integration.

### III. METHOD

This section presents the proposed PGVMS framework for generate mIHC images from H&E images, as shown in Fig. 3. The PGVMS framework comprises three key components designed to achieve optimal virtual staining performance. First, we introduce a pathological semantics-style guided (PSSG) generator that employs prompt-based control to enable efficient multi-stain generation within a single unified model. To ensure pathological fidelity, the framework incorporates two specialized learning strategies: (1) protein-aware learning strategy (PALS) that maintains protein expression consistency across staining modalities, and (2) prototype-consistent learning strategy (PCLS) that enhances high-protein expression region alignment with established pathological prototypes. Together, these strategies guarantee the preservation of critical pathological features between virtually generated and physically stained IHC images.

#### A. Pathological Semantics-Style Guided Generator

Our framework enables efficient multi-stain generation through semantic prompt control, leveraging CONCH’s pathology-specific embeddings trained on 1.17 million IHC image-text pairs [26]. Given text prompt  $T$  (e.g., “H&E to Her2 stained image”), we first extract its base representation:

$$T_b = \text{CONCH}(T) \quad (1)$$

where  $T$  represents the natural language prompt and  $T_b$  captures its general IHC-related semantics. This foundation model embedding provides crucial prior knowledge about biomarker expression patterns and their pathological significance.

To better align embeddings with individual tumor characteristics, we develop an adaptive image-conditioned bias modulation approach. The H&E image features  $X = G_{enc}(I)$  are processed through dual two pooling branches:

$$B_i = \text{Conv}(\text{Cat}(\text{MLP}(\text{AvgPool}(X)), \text{MLP}(\text{MaxPool}(X)))) \quad (2)$$

The average pooling branch captures global tissue architecture, while max pooling emphasizes local cellular abnormalities. Their concatenation and subsequent convolution yield a tumor-specific bias term  $B_i$  that refines the prompt embedding:

$$T_i = T_b + B_i \quad (3)$$

This adjustment ensures the staining process adapts to both the semantic prompt and the unique morphological context of each high-protein expression region.

The prompt guided style normalization (PGSN) module then modulates the staining process through:

$$\text{PGSN}(X) = \gamma \cdot (\rho \cdot \text{IN}(X) + (1 - \rho) \cdot \text{LN}(X)) + \beta \quad (4)$$

where  $\gamma, \beta = \text{Conv}(T_i)$  transform semantic embeddings into stain-specific parameters, and  $\rho$  automatically balances instance normalization (preserving local staining patterns) against layer normalization (maintaining global tissue structure). This adaptive mixture respects both prompt-derived staining styles and inherent tissue organization.

After  $N$  alternating residual and PGSN blocks, the decoder generates the target stain:

$$K^F = G_{dec}(\underbrace{\text{PGSN}(\text{Res}(\dots \text{PGSN}(\text{Res}(X))))}_{N \text{ layers}}) \quad (5)$$

The complete architecture achieves two key innovations: First, it bridges general pathological knowledge from foundation models with case-specific high-protein expression characteristics through adaptive prompt tuning. Second, the hybrid normalization strategy respects both semantic staining directives and biological tissue constraints.

#### B. Protein-Aware Learning Strategy

In IHC staining, target proteins are typically detected through enzyme-conjugated antibodies, with horseradish peroxidase being commonly employed [3]. DAB chromogen forms a brown precipitate with peroxidase, allowing protein quantification via DAB channel optical density. Based on these and Chen et al. [13], PALS initially employs focal optical density mapping to quantify protein distribution in both generated and ground truth images, then applies multi-level protein awareness to enforce biochemical constraints across three hierarchical levels.

1) *Focal Optical Density Mapping*: Firstly,  $K^R$  and  $K^F$  undergo subsequent processing to get the FOD. The optical density (OD) provides a quantitative measure of stain concentration according to the Lambert-Beer law [27]:

$$OD_C = -\log_{10}(K_C/K_{0,C}) = A * c_C \quad (6)$$

where  $K_{0,C}$  and  $K_C$  represent the incident and transmitted light intensities respectively for channel  $C$ ,  $A$  denotes the stain amount, and  $c_C$  is the absorption factor.

Traditional color deconvolution enables DAB stain separation. The stain concentrations are obtained through:

$$S = M^{-1} \cdot OD \quad (7)$$

where  $M \in R^{3 \times 3}$  is the stain matrix containing absorption coefficients,  $S \in R^3$  represents stain concentration vectors.

Only selecting DAB channel transform to standard OD:

$$D = M_{DAB} \cdot S_{DAB} \quad (8)$$

However, the typically small protein expression regions relative to normal tissue create a severe class imbalance. To

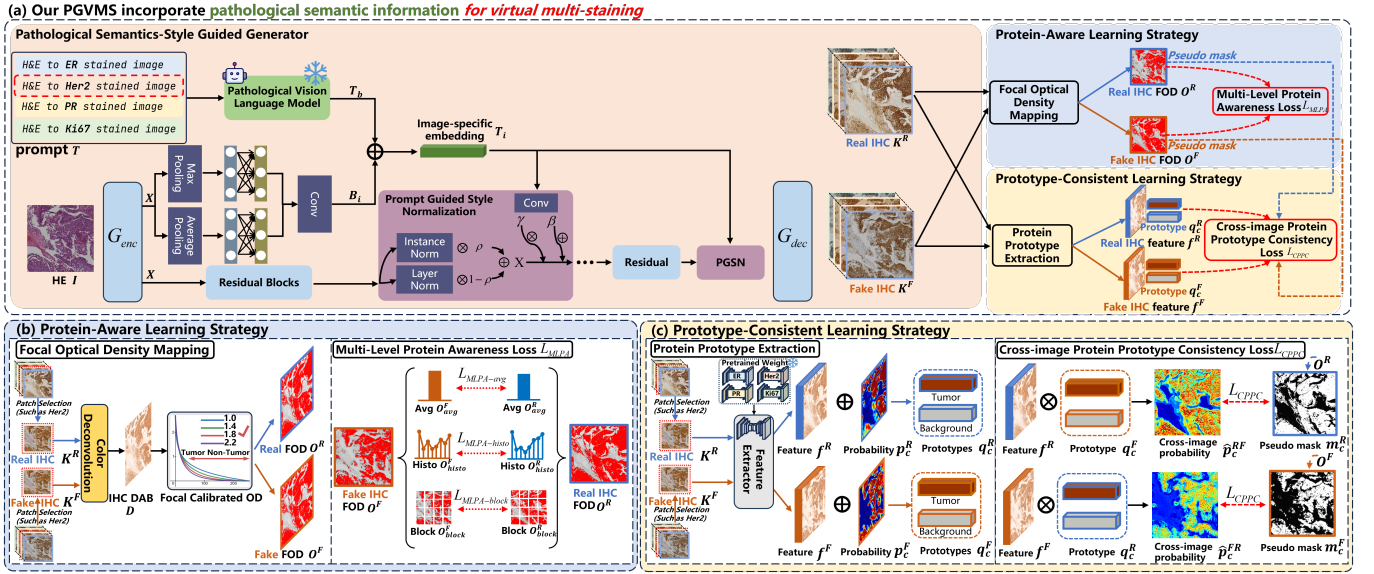


**Fig. 3:** The framework of PGVMS. (a) Overall architecture of PGVMS, including the pathological semantics–style guided (PSSG) generator and schematic overviews of the protein-aware learning strategy (PALS) and the prototype-consistent learning strategy (PCLS). (b) and (c) show detailed illustrations of PALS and PCLS in the bottom row, highlighting their key components and operations.

address this, we introduce a focal optical density (FOD) transformation that emphasizes protein expression regions while suppressing normal tissue:

$$O_C = (-\log_{10}((D_C)/D_{0,C}))^\alpha \quad (9)$$

where  $\alpha > 1$  is a tunable focusing parameter. As shown in Fig. 3(b), increasing  $\alpha$  enhances protein expression region emphasis, with  $\alpha = 1.8$  providing optimal performance in our experiments.

**2) Multi-Level Protein Awareness:** The multi-level protein awareness (MLPA) loss enforces protein expression consistency between generated ( $O^F$ ) and real ( $O^R$ ) IHC images through a hierarchical constraint framework operating at three biologically meaningful spatial scales:

**Global Protein Expression Constraint:** At the macroscopic level, we constrain the overall staining intensity while allowing for natural biological variations:

$$L_{MLPA-avg} = \begin{cases} \|\Delta O\|_2, & \text{if } |\Delta O| \geq \beta \cdot O_{avg}^R \\ 0, & \text{if } |\Delta O| < \beta \cdot O_{avg}^R \end{cases} \quad (10)$$

where  $\Delta O = O_{avg}^F - O_{avg}^R$  quantifies the mean intensity difference between generated and real images, and  $\beta = 0.2$  provides a 20% tolerance threshold that accommodates acceptable clinical variations in staining intensity while preserving diagnostically significant differences.

**Histogram Distribution Alignment:** The histogram term ensures proper representation of all protein expression levels by comparing normalized intensity distributions across  $N_h = 20$  bins:

$$L_{MLPA-histo} = \frac{1}{N_h} \sum_{i=1}^{N_h} \|O_{histo_i}^F - O_{histo_i}^R\|_2 \quad (11)$$

This constraint operates on the complete dynamic range of staining intensities, maintaining proportional representation of clinically relevant expression levels including weak positive regions (0 and 1+), moderate expression (2+), and strong over-expression (3+). The bin-wise comparison prevents common artifacts such as intensity clustering or unrealistic expression distributions.

**Regional Pattern Consistency:** The regional consistency term preserves local biomarker expression patterns through  $N_b = 16$  non-overlapping image blocks:

$$L_{MLPA-block} = \frac{1}{N_b} \sum_{i=1}^{N_b} \|O_{block_i}^F - O_{block_i}^R\|_2 \quad (12)$$

This spatial constraint ensures proper maintenance of protein expression heterogeneity patterns, accurate localization of biomarker hotspots, and prevention of unrealistic expression mosaicism. The block-wise comparison mimics pathologists' regional analysis workflow during diagnostic evaluation.

The complete MLPA loss integrates these components:

$$L_{MLPA} = L_{MLPA-avg} + L_{MLPA-histo} + L_{MLPA-block} \quad (13)$$

### C. Prototype-Consistent Learning Strategy

To address the challenge of spatial misalignment between generated and reference IHC images, we propose PCLS, a method grounded in the biological principle that protein expression content remains intrinsically consistent across different staining modalities of the adjacent patches. The PCLS first extracts protein prototypes and features from both generated and reference images through protein prototype extraction, then enforces bidirectional cross-image protein prototype consistency.

1) *Protein Prototype Extraction*: For each IHC stain type, the prototype extraction process utilizes a corresponding frozen pretrained segmentation UNet to analyze both generated ( $K^F$ ) and real ( $K^R$ ) IHC images through three sequential operations.

First, the UNet encoder-decoder architecture processes each image to extract high-dimensional feature maps  $f^F, f^R \in \mathbb{R}^{H \times W \times D}$  from its penultimate layer:

$$f^F, f^R = \text{UNet}_{\text{penultimate}}(K^F, K^R) \quad (14)$$

Second, the final UNet layer outputs pixel-wise classification probabilities  $p_c^F, p_c^R$  through softmax activation, quantifying protein expression ( $c = 1$ ) versus normal ( $c = 0$ ) tissue likelihoods.

$$p_c^F, p_c^R = \text{softmax}(\text{UNet}_{\text{final}}(K^F, K^R)) \quad (15)$$

where  $c \in \{\text{protein expression region, normal tissue}\}$  indicates the tissue class.

Third, the prototype computation applies confidence-aware feature aggregation by combining the probability maps with their corresponding features:

$$q_c^F = \frac{\sum_i p_c^F(i) \cdot f^F(i)}{\sum_i p_c^F(i)}, q_c^R = \frac{\sum_i p_c^R(i) \cdot f^R(i)}{\sum_i p_c^R(i)} \quad (16)$$

2) *Cross-image Protein Prototype Consistency*: The cross-image consistency mechanism enforces bidirectional semantic alignment through cosine similarity measures:

$$\hat{s}_c^{FR} = \frac{f^F \cdot q_c^R}{\|f^F\| \cdot \|q_c^R\|}, \hat{s}_c^{RF} = \frac{f^R \cdot q_c^F}{\|f^R\| \cdot \|q_c^F\|} \quad (17)$$

These similarity metrics are converted to probability distributions via softmax normalization:

$$\hat{p}_c^{FR} = \frac{e^{\hat{s}_c^{FR}}}{\sum_c e^{\hat{s}_c^{FR}}}, \hat{p}_c^{RF} = \frac{e^{\hat{s}_c^{RF}}}{\sum_c e^{\hat{s}_c^{RF}}} \quad (18)$$

The complete cross-protein prototype consistency (CPPC) loss integrates these bidirectional constraints:

$$L_{CPPC} = \frac{1}{C \times H \times W} \sum_{i=1}^{H \times W} \sum_{c=1}^C (L_{FR}(i, c) + L_{RF}(i, c)) \quad (19)$$

where the individual loss components measure the deviation between predicted and actual protein regions:

$$L_{FR}(i, c) = \|\hat{p}_c^{FR}(i) - m_c^F(i)\|_2$$

$$L_{RF}(i, c) = \|\hat{p}_c^{RF}(i) - m_c^R(i)\|_2$$

where  $m_c^F(i)$  and  $m_c^R(i)$  are derived from  $O^F$  and  $O^R$ , respectively. This formulation simultaneously ensures: (1) cross-modality protein morphology consistency, (2) robustness to staining variations, (3) stain-invariant feature learning, and (4) balanced bidirectional constraint enforcement.

#### D. Other Loss Function

The adversarial loss encourages the generated image  $K^F$  to be indistinguishable from the real image  $K^R$ . It is formulated as:

$$L_{adv} = \mathbb{E}_{K^R} [\log D(K^R)] + \mathbb{E}_{K^F} [\log(1 - D(K^F))], \quad (20)$$

where  $D(\cdot)$  denotes the discriminator,  $K^F$  is the generated image (fake), and  $K^R$  is the real image (ground truth). This loss encourages the generator to produce outputs that are realistic and indistinguishable from real samples.

The NCE loss [5], [28] aims to preserve content consistency across image translation by maximizing mutual information between corresponding patches in the input and output images. It is formulated as a patch-based InfoNCE objective [28]:

$$L_{NCE} = -\log \frac{\exp(\hat{z}_Y \cdot z_X / \tau)}{\exp(\hat{z}_Y \cdot z_X / \tau) + \sum_{n=1}^N \exp(\hat{z}_Y \cdot \hat{z}_X^n / \tau)}, \quad (21)$$

where  $\hat{z}_Y$  is the embedding of a patch in the output image (anchor),  $z_X$  is the corresponding input patch embedding (positive),  $\hat{z}_X^n$  are embeddings of non-corresponding patches (negatives), and  $\tau$  is a temperature hyperparameter controlling the sharpness of the softmax distribution.

The structural similarity (SSIM) loss encourages the generated image  $K^F$  to preserve the structural information of the real image  $K^R$ :

$$L_{SSIM} = 1 - \text{SSIM}(K^F, K^R), \quad (22)$$

where  $\text{SSIM}(\cdot, \cdot)$  computes the structural similarity index between two images. Minimizing  $L_{SSIM}$  promotes preservation of luminance, contrast, and structural patterns in the generated image.

The gaussian pyramid (GP) loss [8] enhances multi-scale consistency between generated and ground truth images, relaxing the strong constraints of the standard L1 loss.

The loss at scale  $i$  is defined as:

$$S_i = \mathbb{E}_{x,y,z} [\|Gaussian_i(K^R) - Gaussian_i(K^F)\|_1] \quad (23)$$

where  $Gaussian_i$  denotes the Gaussian filtering operation at scale  $i$ ,  $K^F$  is the output image,  $K^R$  is the ground truth.

The overall multi-scale loss is formulated as a weighted sum across scales:

$$L_{GP} = \sum_i \lambda_i S_i \quad (24)$$

where  $\lambda_i$  represents the weight for scale  $i$ .

#### E. Overall Loss Function

The overall learning objective is as follows:

$$L_{total} = L_{adv} + L_{NCE} + \lambda_M L_{MLPA} + \lambda_C L_{CPPC} + \lambda_S L_{SSIM} + \lambda_G L_{GP} \quad (25)$$

where  $L_{MLPA}$ ,  $L_{CPPC}$ ,  $L_{GP}$  focus on pathological consistency, with  $L_{GP}$  originating from [8].  $L_{adv}$ ,  $L_{NCE}$ ,  $L_{SSIM}$  contribute to image quality enhancement.

### IV. EXPERIMENTS AND RESULTS

Our method achieves superior performance on both MIST and IHC4BC datasets for H&E to IHC multi-stain transfer, enabling efficient prompt-guided virtual staining of multiple biomarkers. The comparative experimental results show that our method achieve the virtual multiple staining with prompt guided and outperforms other existing methods.

## A. Datasets

1) *MIST dataset*: The MIST dataset [10] provides precisely aligned H&E-IHC image pairs for four critical breast cancer biomarkers (Ki67, ER, PR, and HER2). All image patches are non-overlapping 1024×1024 pixels, with substantial training pairs per stain (4,161-4,642) from 56-64 whole slide images (WSIs), each accompanied by a standardized test set of 1,000 image pairs.

2) *IHC4BC dataset*: The IHC4BC dataset [29] offers larger-scale aligned H&E-IHC pairs for the same four biomarkers, containing approximately 90,000 total patches at 1000×1000 resolution. With 52-60 WSIs per stain, it provides significantly more training data (16,995-26,395 pairs per biomarker) while maintaining the same 1,000-pair test set standardization.

Both datasets maintain overall structural alignment despite minor local deformations, serving as comprehensive benchmarks for computational pathology research.

## B. Implementation Details

We implement our framework using PyTorch on an NVIDIA RTX A6000 GPU. Building upon the CUT framework [5], we employ a ResNet-6Blocks architecture for the generator and a PatchGAN discriminator [4]. The model is trained with random 512×512 patches using a batch size of 1. Optimization is performed using Adam with a fixed learning rate of  $1 \times 10^{-4}$  for 80 epochs. The loss weighting parameters are set as follows:  $\lambda_M = 1.0$ ,  $\lambda_C = 2.5$ ,  $\lambda_S = 0.05$ , and  $\lambda_G = 10.0$ .

During training, the uniplex IHC data are used as image-text pairs to train the prompt-guided virtual staining model. We set the batch size to 1 to ensure that each single-stain IHC image is paired with its corresponding stain-type text label (e.g., “HER2 stain”, “Ki67 stain”, etc.) and input simultaneously into the language model. This setup allows the model to learn from multiple one-to-one image-text pairs during training, while ultimately enabling a one-to-many virtual staining capability at inference.

## C. Evaluation Metrics

Our validation employs a three-level quantitative assessment framework evaluating image quality, pathological correlation, and perceptual consistency. At the image quality level, we measure peak signal-to-noise ratio (PSNR) and structural similarity index measure (SSIM). The pathological correlation level assesses integrated optical density (IOD) [9] and Pearson correlation coefficient (Pearson-R) [11], while the perceptual consistency level evaluates Fréchet inception distance (FID) and deep image structure and texture similarity (DISTS).

1) *SSIM*: In image translation tasks, SSIM is often used to evaluate image quality, primarily to measure the similarity of different images in brightness, contrast, and structure.

2) *PSNR*: As a widely used objective image quality metric, PSNR measures the differences between images by comparing the ratio of signal to noise.

3) *IOD*: IOD quantifies the difference in total protein expression between generated (*test*) and GT (*label*) images.

$$IOD = \sum_{i \in \Omega_{test}} OD_i^{test} - \sum_{i \in \Omega_{label}} OD_i^{label} \quad (26)$$

where  $\Omega$  denotes dataset,  $OD_i$  represents optical density at image  $i$ .

4) *Pearson-R*: Pearson-R evaluates protein expression pattern consistency between generated image and label.

$$Pearson-R = \frac{\sum_{i=1}^I (OD_i^{test} - \bar{OD}^{test})(OD_i^{label} - \bar{OD}^{label})}{\sqrt{\sum_{i=1}^I (OD_i^{test} - \bar{OD}^{test})^2 \sum_{i=1}^I (OD_i^{label} - \bar{OD}^{label})^2}} \quad (27)$$

5) *FID*: FID quantifies the similarity between generated and real images by comparing their feature from Inception V3.

6) *DISTS*: DISTS is a deep learning-based perceptual metric that quantifies image similarity by comparing multi-level structural and textural features extracted through VGG16.

## D. Comparative Results and Analysis

In this section, we compare the performance of our method to other SOTA methods quantitatively and qualitatively based on the MIST and IHC4BC datasets. The compared methods can be broadly classified into two parts: (1) One-to-one virtual staining methods, including Pix2Pix [4], CycleGAN [6], CUT [5], PyramidP2P [8], ASP [10], TDKStain [12], PSPStain [13], DDBM [21] and UNSB [20]; (2) One-to-many virtual staining methods, including ControlNet [19], VIMs [16] and UMDST [15].

1) *Quantitative Assessment*: Empirical results (Tables I and II) demonstrate our method’s superiority in pathological correlation and perceptual consistency, while conventional image quality metrics (PSNR and SSIM) show limited improvement due to inherent structural mismatches between the two staining modalities in the dataset [8]. As detailed in Section V-B with Table XIII, PSNR and SSIM provide only reference values rather than conclusive evaluation criteria.

We then evaluate pathological correlation (IOD and Pearson-R) in terms of variation in total protein expression levels and consistency of expression changes, respectively. For total protein expression levels, as shown in Tables I and II pathology columns, huge variation in IOD is obtained with Pix2Pix, ASP, ControlNet and PyramidP2P, demonstrating their weakness in preserving protein expression from the source images [9]. While other models show better preservation of protein expression levels in stain transfer, our method achieves the best IOD. Furthermore, PGVMS achieves the highest Pearson-R score in both datasets, and this indicates that each generated image closely resembles the ground truth in terms of pathological correlation. These superior IOD and Pearson-R performance metrics of PGVMS can be attributed to the innovative components: PALS maintains protein expression levels matching ground truth, preserving pathological semantics, while PSSG integrates CONCH’s semantic embeddings during stain transfer to ensure structural and biochemical fidelity.

Finally, we evaluate the visual perception (FID and DISTS). As shown in Tables I and II perception columns, our method achieved the lowest FID and DISTS metrics, demonstrating the most realistic stain transformation and tissue structure preservation for pathological diagnosis. This performance advantage stems from PCLS’s design which enforces consistent feature

**TABLE I: COMPARISON OF VIRTUAL STAINING PERFORMANCE ON MIST DATASET. THE BEST SCORES ARE IN BOLD. MODELS ARE GROUPED INTO ONE-TO-ONE AND ONE-TO-MANY CATEGORIES.**

Type	Method	HER2						ER					
		Quality (reference)		Pathology		Perception		Quality (reference)		Pathology		Perception	
		PSNR $\uparrow$	SSIM $\uparrow$	IOD $\times 10^7$	Pearson-R $\uparrow$	FID $\downarrow$	DISTS $\downarrow$	PSNR $\uparrow$	SSIM $\uparrow$	IOD $\times 10^7$	Pearson-R $\uparrow$	FID $\downarrow$	DISTS $\downarrow$
One-to-one	CycleGAN [6]	12.2042	0.1588	+4.5848	0.1995	63.8952	0.2864	13.2516	0.2187	-1.6250	0.2916	54.1309	0.2730
	Pix2Pix [4]	12.9840	0.1676	-2.5782	0.2986	84.3667	0.2699	<b>14.7293</b>	0.2200	-5.8452	0.6307	90.6261	0.3050
	CUT [5]	13.8998	0.1680	-2.9478	0.7164	53.2911	0.2641	14.2172	0.2201	-4.5073	0.5841	45.8074	0.2630
	ASP [10]	14.1841	0.2004	-5.7422	0.0659	50.8364	0.2517	14.2088	0.2178	-4.5875	0.4802	54.7745	0.2705
	PyramidP2P [8]	<b>14.9122</b>	0.1995	-4.5285	0.6894	91.3455	0.2628	14.2062	0.2023	-4.2775	0.7418	92.9292	0.2703
	TDKStain [12]	14.7620	0.1901	-3.1244	0.8147	62.8442	0.2515	14.3451	0.2113	-2.6321	0.8466	46.7817	0.2483
	PSPStain [13]	14.1948	0.1876	-2.5491	0.8303	<b>41.3439</b>	0.2541	14.5718	0.2143	-2.0571	0.8763	39.8844	0.2431
	DDBM [21]	14.7785	0.2156	-6.4420	-0.0228	201.5442	0.3426	14.6963	0.2368	-7.6428	0.1280	191.6672	0.3336
UNSB [20]	13.2797	0.2121	-1.8809	0.3141	54.6514	0.3015	13.3957	0.2452	-1.5399	0.3981	39.1415	0.2955	
One-to-many	ControlNet [19]	8.6754	0.1658	+3.2796	0.0080	121.8161	0.3882	8.4172	0.1564	+19.2318	0.0505	155.9284	0.3499
	VIMs [16]	13.9114	0.1953	-7.0886	0.3049	130.5218	0.3077	14.1536	0.1969	-2.9966	0.0434	97.3877	0.2979
	UMDST [15]	12.6934	<b>0.2181</b>	1.7366	0.1037	71.4340	0.3124	13.6387	<b>0.2528</b>	-1.5309	0.4156	59.9249	0.3122
	PGVMS	13.9246	0.1769	<b>-0.4390</b>	<b>0.8548</b>	44.4247	<b>0.2336</b>	14.3583	0.2072	<b>-0.5193</b>	<b>0.8902</b>	<b>36.5734</b>	<b>0.2299</b>
Type	Method	PR						Ki67					
		Quality (reference)		Pathology		Perception		Quality (reference)		Pathology		Perception	
		PSNR $\uparrow$	SSIM $\uparrow$	IOD $\times 10^7$	Pearson-R $\uparrow$	FID $\downarrow$	DISTS $\downarrow$	PSNR $\uparrow$	SSIM $\uparrow$	IOD $\times 10^7$	Pearson-R $\uparrow$	FID $\downarrow$	DISTS $\downarrow$
One-to-one	CycleGAN [6]	13.8537	0.2040	-6.1662	0.2229	75.4442	0.2736	13.9144	0.2186	-2.6220	0.2726	46.1386	0.2538
	Pix2Pix [4]	<b>15.0557</b>	0.2338	-5.8785	0.7201	80.4802	0.3101	14.6090	0.2360	-2.0715	0.5560	93.7772	0.2568
	CUT [5]	14.3480	0.2209	-2.8106	0.7032	41.2165	0.2601	14.4081	0.2095	-2.2291	0.4878	42.0596	0.2520
	ASP [10]	14.1200	0.2111	-5.7499	0.5557	47.8368	0.2547	14.5852	0.2286	-2.3507	0.4562	50.9120	0.2462
	PyramidP2P [8]	14.2600	0.2097	-5.9274	0.7318	85.6816	0.2718	13.9477	0.2231	-0.6542	0.5877	87.8460	<b>0.2417</b>
	TDKStain [12]	14.7783	0.2320	-2.5365	0.8658	56.2217	0.2534	14.6585	0.2391	-1.0361	0.7473	58.5757	0.2454
	PSPStain [13]	14.8824	0.2347	-3.5771	0.8661	38.3390	0.2454	14.2602	0.2415	<b>-0.0671</b>	0.7718	37.5574	0.2607
	DDBM [21]	13.4919	0.2242	-6.4651	0.4206	168.8190	0.3087	14.1996	0.2357	-1.8336	0.4149	158.1006	0.2909
UNSB [20]	13.7457	<b>0.2572</b>	-1.2455	0.3906	41.3750	0.3136	14.1265	0.2722	-0.3999	0.3981	<b>33.2999</b>	0.2836	
One-to-many	ControlNet [19]	9.0790	0.1508	+5.6869	0.0928	136.1356	0.3710	10.2877	<b>0.2831</b>	+6.4306	0.2751	292.4799	0.3955
	VIMs [16]	13.3384	0.1591	-4.2534	0.0341	115.3529	0.3069	13.7166	0.1906	-6.0985	0.2202	110.7464	0.3002
	UMDST [15]	13.7066	0.2515	-1.7874	0.4968	59.4099	0.3039	13.8163	0.2595	+0.7868	0.2642	94.9168	0.3174
	PGVMS	14.2510	0.2000	<b>+0.7815</b>	<b>0.9126</b>	<b>34.9099</b>	<b>0.2300</b>	<b>14.8344</b>	0.2285	-1.1125	<b>0.8018</b>	36.3537	0.2439

**TABLE II: COMPARISON OF VIRTUAL STAINING PERFORMANCE ON IHC4BC DATASET. THE BEST SCORES ARE IN BOLD. MODELS ARE GROUPED INTO ONE-TO-ONE AND ONE-TO-MANY CATEGORIES.**

Type	Method	HER2						ER					
		Quality (reference)		Pathology		Perception		Quality (reference)		Pathology		Perception	
		PSNR $\uparrow$	SSIM $\uparrow$	IOD $\times 10^8$	Pearson-R $\uparrow$	FID $\downarrow$	DISTS $\downarrow$	PSNR $\uparrow$	SSIM $\uparrow$	IOD $\times 10^7$	Pearson-R $\uparrow$	FID $\downarrow$	DISTS $\downarrow$
One-to-one	CycleGAN [6]	10.1229	0.0930	+1.9836	0.3071	143.8269	0.3385	17.3148	0.4406	+0.8744	0.3878	50.9366	0.2545
	Pix2Pix [4]	11.3910	0.1228	-0.9739	0.6214	117.3533	0.3027	20.7537	0.4931	-1.0956	0.2171	129.9073	0.3050
	CUT [5]	10.9131	0.1227	-1.2030	-0.0613	63.3108	0.2657	19.4466	0.4745	-1.0011	0.6705	41.8358	0.2618
	ASP [10]	11.2034	0.1245	-1.1742	-0.0988	63.9972	0.2658	19.5277	0.4834	-0.6886	0.1810	37.9753	0.2644
	PyramidP2P [8]	10.8870	0.1325	-0.5059	0.4234	113.6700	0.3612	<b>21.2933</b>	<b>0.5606</b>	-1.3231	0.1230	121.3450	0.4019
	TDKStain [12]	11.0847	0.1263	-0.4522	0.7451	72.6141	<b>0.2498</b>	19.6842	0.4652	-0.5041	0.5925	50.3415	0.2529
	PSPStain [13]	11.1210	0.1213	-0.5439	0.7022	57.0579	0.2585	18.6233	0.4240	-0.2761	0.7651	39.6011	0.2586
	DDBM [21]	<b>11.7847</b>	0.1136	-1.2303	-0.0095	206.7112	0.4091	20.5214	0.4749	-1.3201	0.0103	290.9201	0.3711
UNSB [20]	11.0874	0.1392	-0.6440	0.1654	54.7004	0.3155	19.4668	0.4963	-0.6459	0.3130	61.3214	0.3151	
One-to-many	ControlNet [19]	7.9736	0.1028	+0.6942	0.2747	143.5401	0.3846	7.4402	0.2908	+25.7725	0.0412	235.9315	0.4063
	VIMs [16]	11.3224	0.1226	-1.0667	0.0945	86.0438	0.3693	17.4837	0.4001	-0.8389	0.3534	90.6424	0.3068
	UMDST [15]	11.1742	<b>0.1449</b>	-0.3930	0.4135	65.5618	0.3183	20.5402	0.5346	-1.1084	0.1270	63.3261	0.3448
	PGVMS	11.0508	0.1234	<b>-0.3262</b>	<b>0.7751</b>	<b>53.3853</b>	0.2552	19.7848	0.4750	<b>-0.1098</b>	<b>0.7940</b>	<b>36.8306</b>	<b>0.2326</b>
Type	Method	PR						Ki67					
		Quality (reference)		Pathology		Perception		Quality (reference)		Pathology		Perception	
		PSNR $\uparrow$	SSIM $\uparrow$	IOD $\times 10^7$	Pearson-R $\uparrow$	FID $\downarrow$	DISTS $\downarrow$	PSNR $\uparrow$	SSIM $\uparrow$	IOD $\times 10^7$	Pearson-R $\uparrow$	FID $\downarrow$	DISTS $\downarrow$
One-to-one	CycleGAN [6]	17.9551	0.4544	+1.3643	0.2339	66.0757	0.3113	18.7757	0.3840	+0.8227	0.6277	52.5754	0.2328
	Pix2Pix [4]	23.9329	0.5556	-0.5986	0.1558	116.1813	0.2702	20.5521	0.4413	-0.4839	0.2138	140.2222	0.2914
	CUT [5]	19.0278	0.4882	+0.6367	0.2133	47.5413	0.3153	17.2823	0.3017	-0.5802	0.1187	114.3944	0.3063
	ASP [10]	23.3897	0.5454	-0.5677	-0.0954	42.3880	0.2575	19.1923	0.3849	-0.2544	0.5686	27.0728	0.2272
	PyramidP2P [8]	24.1510	<b>0.6187</b>	-0.5892	0.0479	87.7714	0.3378	20.7354	<b>0.4895</b>	-0.4475	0.3627	63.2432	0.3150
	TDKStain [12]	21.9699	0.5236	-0.2936	0.0073	64.9066	0.2739	19.4341	0.4014	<b>-0.0994</b>	0.8735	38.1665	0.2302
	PSPStain [13]	23.8481	0.5544	-0.5586	0.5877	43.8625	0.2503	18.9546	0.3966	+0.4443	0.8744	32.2626	0.2539
	DDBM [21]	22.5329	0.5293	-5.6605	0.0136	239.2746	0.3284	19.1372	0.3744	-0.3313	0.5537	120.2547	0.3166
UNSB [20]	23.7180	0.5957	-0.5131	0.2865	42.2145	0.3052	20.5115	0.4523	-0.4590	0.7595	35.9533	0.2905	
One-to-many	ControlNet [19]	8.3349	0.2686	+9.6558	0.0084	259.7857	0.4424	8.8441	0.2168	+6.5673	0.6417	252.8057	0.4164
	VIMs [16]	<b>24.2096</b>	0.5438	-0.6146	0.0075	112.9235	0.3357	<b>20.7378</b>	0.3930	-0.5592	0.5227	84.4047	0.3316
	UMDST [15]	22.5452	0.5795	-0.4066	0.0761	45.6025	0.3120	20.1732	0.4651	-0.4733	0.5237	56.5546	0.3003
	PGVMS	22.4371	0.5388	<b>-0.0499</b>	<b>0.7084</b>	<b>40.6377</b>	<b>0.2495</b>	20.3849	0.4191	-0.2256	<b>0.8913</b>	<b>24.4450</b>	<b>0.2208</b>

embedding in latent space, thereby preserving key pathological features in synthesized protein margins and cellular atypia.

2) *Qualitative Assessment*: To further explore the visual differences in the virtual staining, we present the results of our method and other competing methods on MIST dataset in Fig. 4 and IHC4BC dataset in Fig. 6. DeepLIF [30] was used to highlight positive cells (red) and negative cells (blue).

Compared with others, the virtual IHC images generated by our method are most similar with the real IHC images.

Fig. 4 and Fig. 6 reveals that existing methods like CycleGAN, Pix2Pix, and CUT produce IHC images with inaccurate pathological characteristics due to insufficient supervisory information. Moreover, ASP and PyramidP2P contain insufficient pathological characteristics due to the patch-level

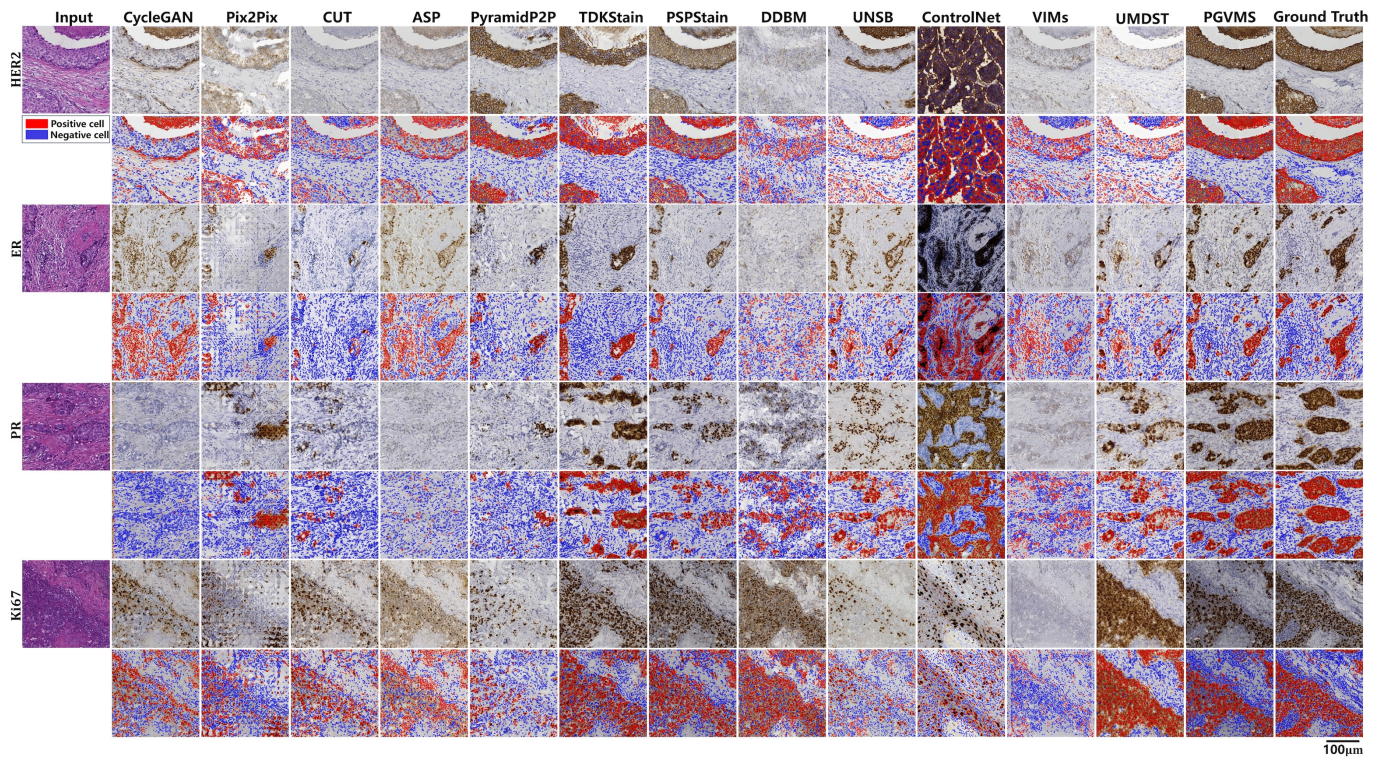


**Fig. 4:** Virtual IHC-stained image results of different methods on the MIST dataset. The first column is the H&E-stained images. Columns 2 to 14 are the images virtually stained by different methods. The last column is the ground truth. The figure also demonstrates virtual IHC results alongside positive cell visualization from DeepLIIF.

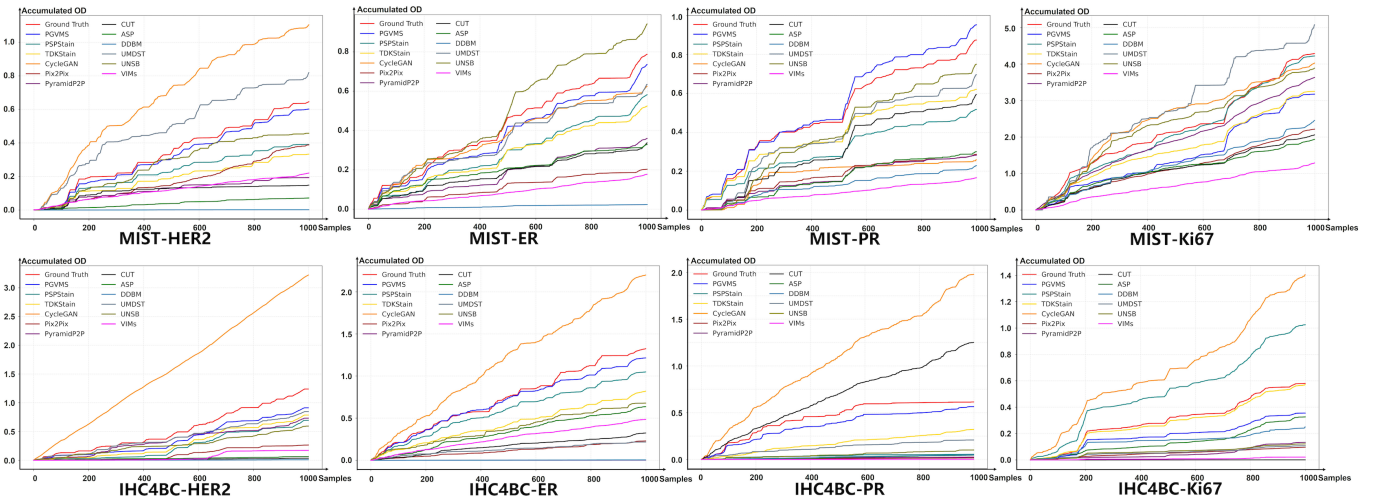


**Fig. 5:** Consistent with the protein progression tendency. The horizontal axis (abscissa) represents the sample index, while the vertical axis (ordinate) denotes the accumulated optical density (OD) value. The figure illustrates the accumulated OD curves of various virtual staining methods for IHC positive regions, comparing the virtual results with the reference IHC images on the MIST and IHC4BC datasets. The results of the ControlNet model are excluded because they deviate significantly from the ground truth.

loss between virtual IHC images and weakly paired ground truth. ControlNet often produces hallucinations due to the lack of sufficient pathological constraints. VIMs and UMDST, as one-to-many methods, lack the precision to identify protein overexpression regions accurately. In contrast, both TDKStain and PSPStain detect the protein expression amount, thus they

maintain strong pathological relevance with real IHC images. However, TDKStain often produces wrong tumor shapes and distributions (Fig. 7), as it fails to accurately capture cellular localization and may introduce spurious cellular artifacts. Meanwhile, PSPStain preserves the tissue structure in H&E-stained images through semantic preservation. Notably, virtual

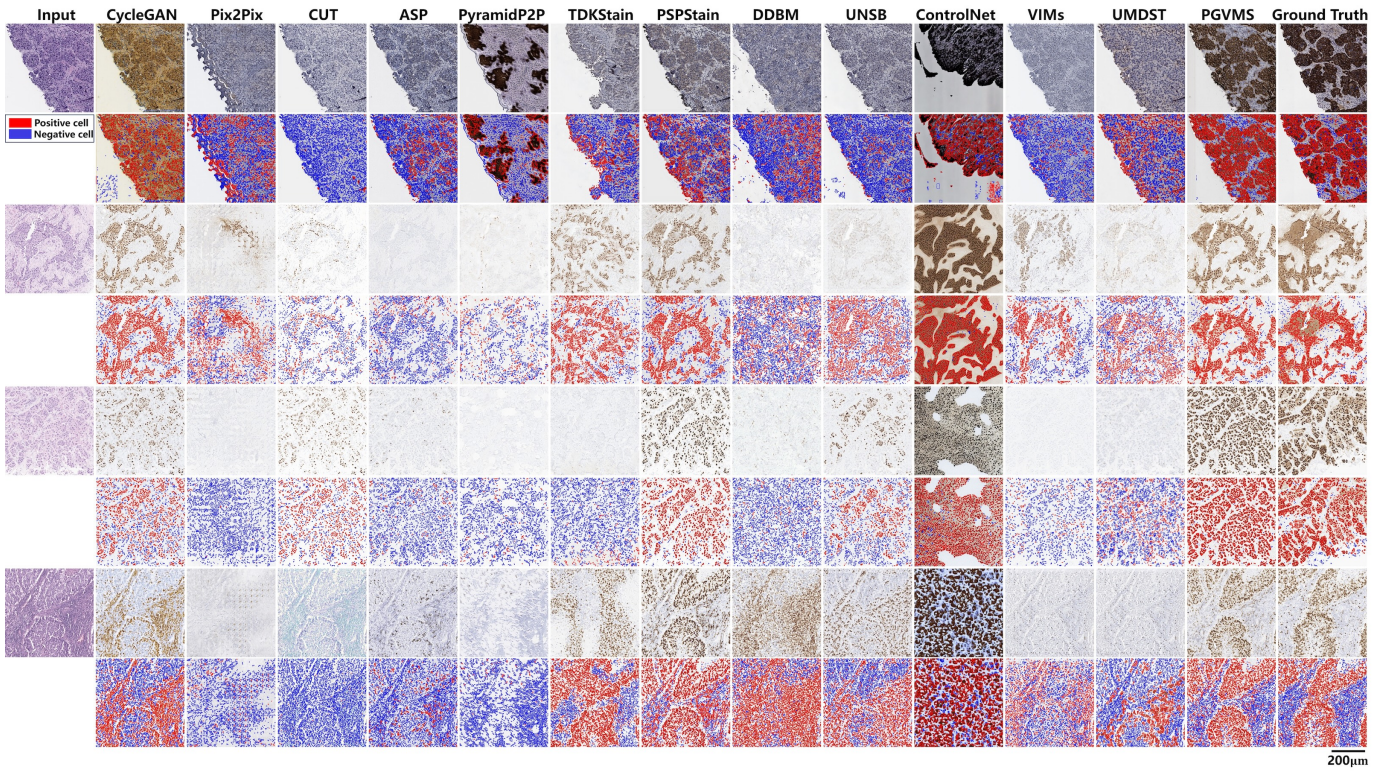


Fig. 6: Virtual IHC-stained image results of different methods on the IHC4BC dataset. The first column is the H&E-stained images. Columns 2 to 14 are the images virtually stained by different methods. The last column is the ground truth. The figure also demonstrates virtual IHC results alongside positive cell visualization from DeepLIF.

IHC images generated by PGVMS exhibit closer similarity to referenced adjacent-layer IHC images by learning pathological semantics—particularly in highlighting small high-protein expression areas missed by other methods.

3) *Protein Expression Analysis*: Typically, pathologists pay more attention to the protein expression level of IHC staining when analyzing IHC images [31]. Therefore, the accuracy of virtual IHC images can be effectively evaluated by studying the correlation between the protein expression level in virtual IHC images and those in real IHC images from adjacent layers.

For each IHC patch, the H channel and the DAB channel can be separated using deconvolution. In the DAB channel, we calculate the tumor expression level for each patch and then accumulate the expression levels across all patches [13], as shown in the line chart (Fig. 5). The red line in the chart represents the cumulative curve of positive protein expression levels for the reference. Notably, CycleGAN (orange) exhibits substantial deviation from the reference (red) trajectory, indicating poor pathological concordance. The results of the ControlNet model are excluded because they deviate significantly from the ground truth. PSPStain (cyan) and TDKStain (yellow) exhibit good consistency. However, our PGVMS (blue) demonstrates the closest approximation to the reference profile across three stain types, visually confirming its superior pathological consistency with authentic IHC results.

4) *Downstream Classification Experiments*: To evaluate the diagnostic value of virtual staining, we assessed the impact of generated IHC images on downstream biomarker classification

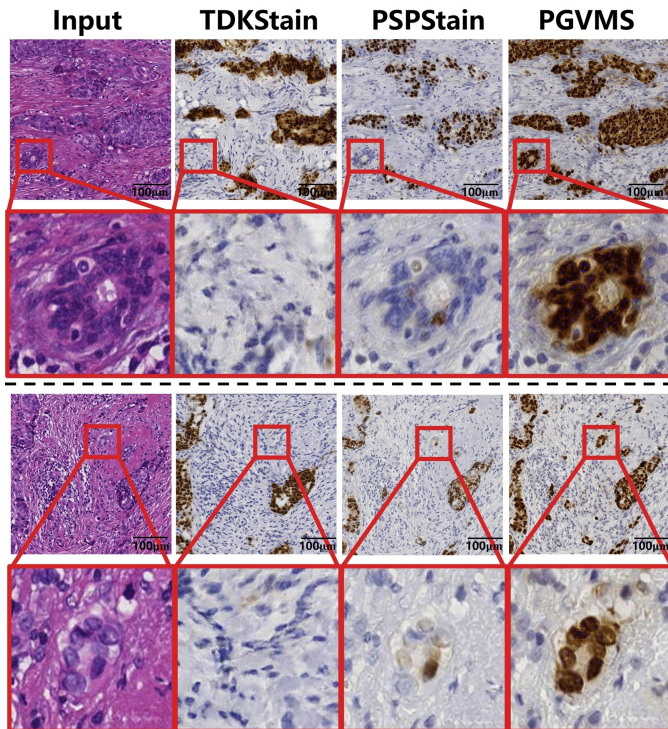
(Table III) using a ViT-B/32 backbone classifier. Separate models were trained for each biomarker—HER2, ER, PR, and Ki67—on the MIST and IHC4BC datasets to measure how well pathological information was preserved.

TABLE III: Classification accuracy (%) of virtual staining results on MIST and IHC4BC datasets. HER2: 4-class (0, 1+, 2+, 3+); ER, PR, Ki67: binary (negative/positive). Models are grouped into one-to-one and one-to-many categories.

Method	MIST				IHC4BC			
	HER2	ER	PR	Ki67	HER2	ER	PR	Ki67
CycleGAN	0.453	0.570	0.534	0.767	0.495	0.600	0.479	0.771
Pix2Pix	0.490	0.671	0.671	0.847	0.422	0.595	0.666	0.613
CUT	0.457	0.610	0.664	0.807	0.258	0.573	0.492	0.565
ASP	0.378	0.623	0.637	0.759	0.256	0.547	0.559	0.799
PyramidP2P	0.587	0.695	0.705	0.842	0.505	0.497	0.640	0.686
TDKStain	<b>0.642</b>	<b>0.798</b>	<b>0.812</b>	<b>0.857</b>	<b>0.541</b>	<b>0.667</b>	0.571	<b>0.834</b>
PSPStain	<b>0.647</b>	0.763	0.768	0.844	0.474	0.596	<b>0.750</b>	0.763
DDBM	0.420	0.584	0.577	0.634	0.449	0.534	0.629	0.754
UNSB	0.450	0.642	0.611	0.802	0.397	0.563	0.626	0.782
ControlNet	0.329	0.673	0.537	0.844	0.470	0.558	0.352	0.599
VIMS	0.309	0.652	0.561	0.795	0.326	0.626	0.657	0.578
UMDST	0.419	0.572	0.655	0.843	0.251	0.462	0.640	0.687
PGVMS	0.617	<u>0.772</u>	<b>0.818</b>	0.740	<u>0.535</u>	<u>0.627</u>	<u>0.678</u>	<b>0.865</b>

HER2 was treated as a four-class problem (0, 1+, 2+, 3+) based on cumulative OD thresholds of 500, 2000, and 5000. ER and PR were binarized at 1000, and Ki67 at 2000, following established cutoffs [27]. All automated labels were subsequently reviewed by board-certified pathologists.

As shown in Table III, TDKStain achieves the highest classification accuracy, followed by PGVMS and PSPStain. However, TDKStain shows severe cell localization errors,



**Fig. 7:** Visual comparison illustrating the severe cell spatial misalignment issue in TDKStain results, where virtual staining causes substantial cell displacement relative to the input H&E image. In contrast, our PGVMS method preserves accurate cell spatial localization.

with notable misalignment between the generated IHC and input H&E images (Figure 7), significantly limiting its clinical usability.

**5) Feature-Level Metric Based on Pathological Foundation Model CONCH:** To assess the feature-level alignment of virtual IHC images with clinical pathology, we encode both the generated and ground-truth IHC images using the pre-trained image encoder of CONCH, producing a 512-dimensional feature vector for each image. The CONCH-FID is then calculated as the Fréchet distance between the distributions of these embeddings, capturing how well the generated images preserve high-level, pathology-specific semantic features. As shown in Table IV, our PGVMS method ranks second on the MIST dataset, first on the IHC4BC dataset, and achieves the best overall performance across datasets. In comparison, PSPStain ranks second overall, while ASP comes third. These results highlight PGVMS’s superior ability to generate virtual IHC images that closely replicate the structural and semantic characteristics of authentic clinical slides.

**6) Pathologist-Based Image Quality Evaluation:** To assess the clinical feasibility of our virtual staining results, we invited experienced pathologists to conduct a subjective quality evaluation. Specifically, for each dataset (MIST and IHC4BC), 50 randomly selected patches per stain were scored on a 1–5 scale based on three criteria: cellular localization, staining heterogeneity, and staining intensity. Scores of 3 and above indicate acceptable quality, while scores below 3 are considered

unsatisfactory. As illustrated in Fig. 8 and Fig. 9, the virtual IHC-stained images achieve consistently high quality across all criteria, with mean scores exceeding 3.0 and often approaching 4.0 or higher. On the MIST dataset, ER and PR stains receive the highest scores in both localization and intensity, suggesting that the model effectively preserves nuclear and cytoplasmic structures. On the IHC4BC dataset, HER2 and Ki67 exhibit stable performance across all aspects, demonstrating good generalization to cross-domain and inter-patient variations. Overall, these results confirm that our method generates visually convincing and histologically consistent virtual IHC images, which are well accepted by pathologists and hold strong potential for clinical application.

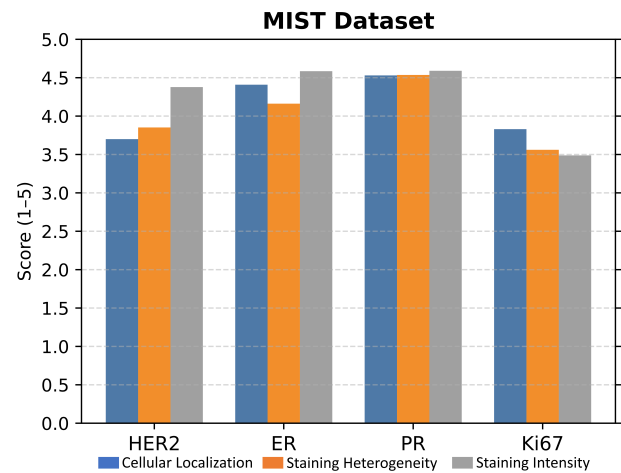


**Fig. 8:** Pathologist evaluation of virtual IHC-stained images on the MIST datasets across three criteria: cellular localization, staining heterogeneity, and staining intensity.

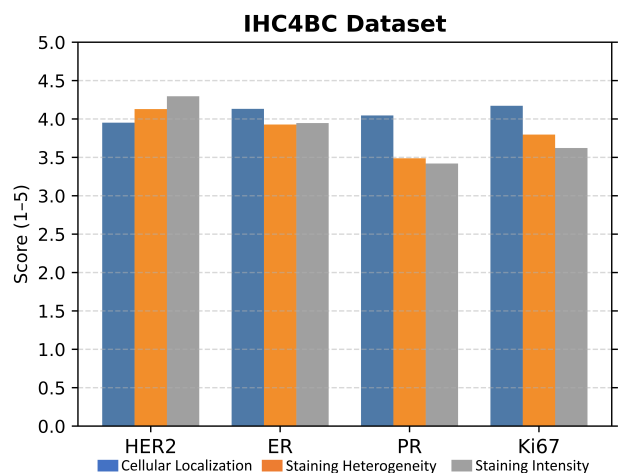


**Fig. 9:** Pathologist evaluation of virtual IHC-stained images on the IHC4BC datasets across three criteria: cellular localization, staining heterogeneity, and staining intensity.

**7) Unified Multiple IHC Virtual Staining Analysis:** Fig. 10 shows the virtual generation of HER2, ER, PR, and Ki67 stained images from H&E images, with each stain exhibiting

**TABLE IV:** Feature-level FID between virtual IHC and ground-truth IHC computed using the pathology foundation model CONCH. Lower values indicate better alignment. The best and second-best results are highlighted in **bold** and underlined, respectively.

Type	Method	MIST					IHC4BC				
		HER2	ER	PR	Ki67	Mean	HER2	ER	PR	Ki67	Mean
One-to-one	CycleGAN	102.1581	52.9350	125.7399	48.0381	82.2178	218.4938	44.1311	81.4923	49.0361	98.2884
	Pix2Pix	95.9983	189.5522	182.9658	216.5276	171.2610	153.2364	105.1925	95.7887	128.3961	120.6534
	CUT	62.6960	39.4071	32.4882	35.4223	42.5034	80.8654	32.3410	39.4285	247.6296	100.0661
	ASP	<u>39.9833</u>	52.4421	38.3425	43.7905	43.6396	76.8791	<u>25.4769</u>	<u>31.9873</u>	<b>20.9709</b>	<u>38.8285</u>
	Pyramid	151.2503	153.7980	145.9719	172.3845	155.8512	237.9637	172.1971	162.0819	106.7118	169.7386
	TDKStain	85.3784	73.2279	98.2533	143.9924	100.2130	<u>49.5412</u>	61.5834	75.3190	52.3977	59.7103
	PSPStain	<b>34.7499</b>	<b>30.8958</b>	32.7645	<b>26.2759</b>	<b>31.1715</b>	<b>47.1362</b>	35.2759	48.1594	36.9802	41.8879
	DDBM	291.1494	281.9772	244.6667	215.1843	258.2444	326.7613	256.5512	258.2804	182.5962	256.0473
	UNSB	61.9792	38.1701	49.4495	36.9417	46.6351	64.6003	69.6588	37.2139	48.7528	55.0565
One-to-many	ControlNet	283.2979	253.5201	317.4814	490.4310	336.1826	322.7134	432.5187	455.0586	434.0198	411.0776
	VIMs	353.5241	240.2728	234.2091	233.9704	265.4941	192.7621	140.0983	177.3091	166.0101	169.0449
	UMDST	154.3398	168.4891	147.7141	254.2693	181.2031	98.5943	116.0732	100.4608	184.7146	124.9607
	PGVMS	55.1115	<u>31.0460</u>	<b>23.5529</b>	<u>29.5545</u>	<u>34.8162</u>	61.7747	<b>24.5485</b>	<b>30.8413</b>	<u>21.8956</u>	<b>34.7650</b>

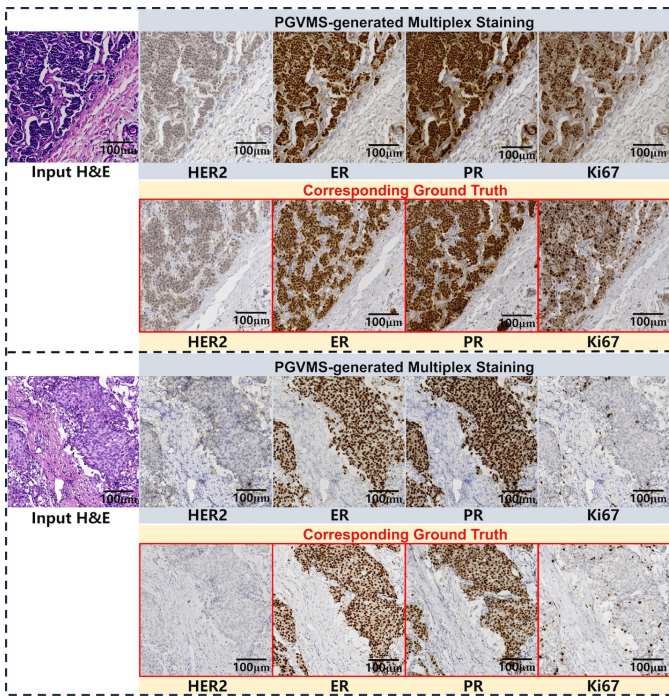


**Fig. 10:** Virtual multiplex IHC generation from H&E-stained input images. For each H&E input, the first row (gray background) displays PGVMS-generated staining for HER2, ER, PR, and Ki-67, and the second row (yellow background) shows the corresponding ground-truth IHC images.

distinct characteristics—for example, the first image shows strong ER, PR, and Ki67 but minimal HER2 expression, while the second shows strong ER and PR with low HER2 and Ki67. These results demonstrate that our method can generate multiple IHC stains simultaneously, aiding breast cancer subtype identification. The multiplex IHC images used for visualization are from the MIST dataset, which is mostly uniplex ( $\sim 77.8\%$ ), with only a small fraction containing 2–4 stains.

### E. Ablation Study and Analysis

1) *Module Ablation:* The proposed PGVMS accurately transforms H&E-stained images into IHC-stained images through three core mechanisms: PALS, PCLS, and the PSSG generator. The baseline, built on the CUT framework, serves as an initial model for stain translation. PALS ensures pathological consistency by preserving protein activation patterns, while PCLS enhances protein realism by enforcing semantic coherence across images. The PSSG generator enables prompt-driven adaptation for multi-stain tasks. Ablation experiments on the MIST dataset (Table V, pathology columns) reveal that PALS exerts a greater impact on pathological consistency. However, with PALS alone, protein characterization remains suboptimal. Consequently, PCLS improves perception metrics and enhances protein realism (Table V, perception columns). When combined with PSSG’s semantic-embedded prompts, these components collectively achieve optimal stain transfer results, demonstrating PGVMS’s state-of-the-art virtual staining capability.

**TABLE V:** ABLATION STUDY OF STAIN TRANSFER PERFORMANCE ON MIST DATASET. THE BEST SCORES ARE HIGHLIGHTED IN BOLD.

Baseline	PALS	PCLS	PSSG	Quality		Pathology		Perception	
				PSNR $\uparrow$	SSIM $\uparrow$	IOD $\times 10^7$	Pearson-R $\uparrow$	FID $\downarrow$	DISTS $\downarrow$
✓				14.2183	0.2046	-3.1237	0.6229	45.6044	0.2598
✓	✓			<b>14.6252</b>	<b>0.2205</b>	-2.3128	0.8436	49.7711	0.2577
✓	✓	✓		14.4773	0.2195	-2.0626	0.8361	39.2908	0.2508
✓			✓	13.7738	0.1905	-5.0098	0.3756	62.5494	0.2709
✓	✓		✓	13.0808	0.1887	-2.9507	0.3998	67.4985	0.2813
✓	✓	✓	✓	14.3421	0.2032	<b>-0.3223</b>	<b>0.8649</b>	<b>38.0654</b>	<b>0.2343</b>

To further explore the visual effects of the PCLS, PALS, and PSSG generator on virtual IHC image generation, we present qualitative ablation results in Fig. 11. As shown in Fig. 11, without the constraints of PALS and PCLS, the model fails to fully utilize the supervisory information provided by adjacent layer IHC images (yellow), resulting in inaccurate pathological characteristics, such as misstained nuclei or cell membranes. PALS effectively maintains the pathological consistency of the

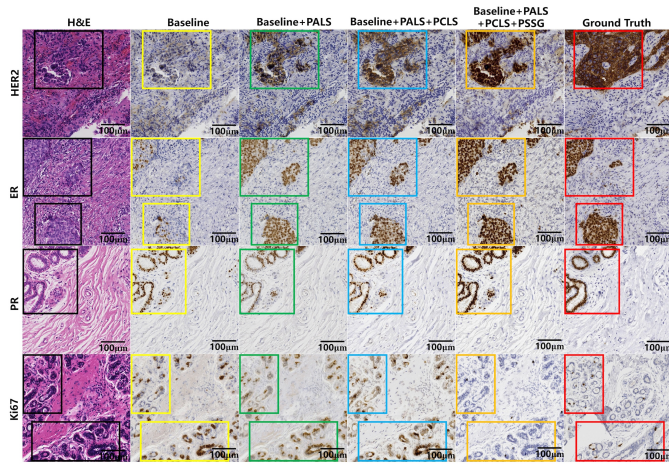


Fig. 11: Visualization of the effects of PALS, PCLS, and PSSG on our PGVMS. The color-coded rectangles indicate regions corresponding to different experimental configurations: black for the input H&E image, yellow for the baseline output, green for baseline + PALS, blue for baseline + PALS + PCLS, orange for baseline + PALS + PCLS + PSSG, and red for the ground truth.

generated images by preserving molecular-level protein activation patterns (green), ensuring that the virtual staining aligns with biological reality. PCLS enhances the realism of the generated tumor regions by enforcing cross-image semantic topology consistency (blue), mitigating spatial misalignment and improving inter-image coherence. PSSG generator enables prompt-driven semantic embedding adaptation across multiple staining tasks (orange), enhancing pathological semantic embedding. When PALS and PCLS are added, the performance improves, but some staining inaccuracies remain, and certain nuclei are still incorrectly stained. When the PSSG generator, PALS, and PCLS are applied simultaneously, the virtual IHC images closely resemble the referenced adjacent layer IHC images (red), achieving the best staining transfer performance.

2) *Guidance Mechanism*: To evaluate how pathological semantic prompts operate within the PSSG generator, we replaced the CONCH model with one-hot encoding guidance and CLIP model guidance. As shown in the Table VI, the minimal IOD indicates superior protein expression consistency, while the relatively low yet high absolute Pearson-R score reflects consistent tumor expression patterns. The outstanding perception metrics demonstrate optimal visual diagnostic fidelity, highlighting CONCH’s capability to deliver robust pathological semantic embeddings for virtual multiplex IHC staining within a unified model.

TABLE VI: ABLATION STUDY OF GUIDANCE MECHANISM ON MIST DATASET. THE BEST SCORES ARE HIGHLIGHTED IN BOLD.

Guidance	Quality		Pathology		Perception	
	PSNR $\uparrow$	SSIM $\uparrow$	IOD $\times 10^7$	Pearson-R $\uparrow$	FID $\downarrow$	DISTS $\downarrow$
One Hot	<b>14.9029</b>	<b>0.2310</b>	-2.1429	<b>0.8729</b>	38.5514	0.2379
CLIP	14.2745	0.1895	-1.4198	0.8678	39.2263	0.2454
CONCH	14.3421	0.2032	<b>-0.3223</b>	0.8649	<b>38.0654</b>	<b>0.2344</b>

3) *Image-Guided Bias Effectiveness*: We evaluated the effect of incorporating instance-specific image-derived bias into the text prompt. As shown in Table VII, adding the bias consistently improves pathology, quality, and perception metrics across all biomarkers, indicating that it enhances semantic alignment and preserves domain-specific features in the virtual stains.

TABLE VII: ABLATION STUDY OF IMAGE-GUIDED BIAS MECHANISM ON MIST DATASET. THE BEST SCORES ARE HIGHLIGHTED IN BOLD.

Method	Quality		Pathology		Perception	
	PSNR $\uparrow$	SSIM $\uparrow$	IOD $\times 10^7$	Pearson-R $\uparrow$	FID $\downarrow$	DISTS $\downarrow$
w/o bias	14.0289	<b>0.2099</b>	-2.2577	0.7400	58.2488	0.2482
w/ bias	<b>14.3421</b>	0.2062	<b>-0.3223</b>	<b>0.8648</b>	<b>38.0654</b>	<b>0.2344</b>

4) *Pooling Strategy in Bias Computation*: We compared max pooling, average pooling, and a combination of both for extracting the image-guided bias. Table VIII shows that combining max and average pooling outperforms either operation alone, suggesting that fusing localized discriminative cues with global contextual information provides a more informative and balanced bias for guiding the virtual staining.

TABLE VIII: ABLATION STUDY OF POOLING STRATEGY ON MIST DATASET. THE BEST SCORES ARE HIGHLIGHTED IN BOLD.

Pooling Strategy	Quality		Pathology		Perception	
	PSNR $\uparrow$	SSIM $\uparrow$	IOD $\times 10^7$	Pearson-R $\uparrow$	FID $\downarrow$	DISTS $\downarrow$
Only Maxpooling	14.5682	<b>0.2184</b>	-1.7611	0.7890	53.5903	0.2522
Only Avgpooling	<b>14.6032</b>	0.2086	-2.4378	0.7607	83.3022	0.2646
Max & Avg Pooling	14.3421	0.2032	<b>-0.3223</b>	<b>0.8648</b>	<b>38.0654</b>	<b>0.2344</b>

5) *Fusion Strategy in PGSN*: We ablated the prompt guidance style normalization (PGSN) against simple addition and cross-attention between the prompt and image feature. Table IX demonstrates that PGSN substantially outperforms these alternatives by adaptively modulating text embeddings with image-derived statistics, leading to stronger semantic alignment and better preservation of pathology-specific features.

TABLE IX: ABLATION STUDY OF FUSION MECHANISM ON MIST DATASET. THE BEST SCORES ARE HIGHLIGHTED IN BOLD.

Guidance	Quality		Pathology		Perception	
	PSNR $\uparrow$	SSIM $\uparrow$	IOD $\times 10^7$	Pearson-R $\uparrow$	FID $\downarrow$	DISTS $\downarrow$
Addition	13.8117	0.1904	-1.5385	0.7942	53.1891	0.2451
Cross Attention	13.8461	0.2028	-2.4021	0.8041	55.5236	0.2438
PGSN	<b>14.3421</b>	<b>0.2032</b>	<b>-0.3223</b>	<b>0.8649</b>	<b>38.0654</b>	<b>0.2344</b>

6) *Normalization Strategy*: We assessed the role of instance normalization (IN) and layer normalization (LN) within PGSN. Table X shows that using both IN and LN achieves the best overall performance, as IN suppresses irrelevant style variations while LN stabilizes global feature distributions, resulting in more accurate and consistent virtual staining.

7) *Sensitivity Analysis of  $\alpha$  in MLPA*: To investigate the influence of  $\alpha$  in MLPA, we conducted an ablation study

**TABLE X:** ABLATION STUDY OF NORMALIZATION STRATEGY ON MIST DATASET. THE BEST SCORES ARE HIGHLIGHTED IN BOLD.

Normalization Strategy	Quality		Pathology		Perception	
	PSNR $\uparrow$	SSIM $\uparrow$	IOD $\times 10^7$	Pearson-R $\uparrow$	FID $\downarrow$	DISTS $\downarrow$
Only IN	14.4614	0.2184	-3.2292	0.7939	69.9662	0.2600
Only LN	<b>15.6425</b>	<b>0.2887</b>	-3.9779	0.7672	153.7774	0.3414
Both IN&LN	14.3421	0.2032	<b>-0.3223</b>	<b>0.8649</b>	<b>38.0654</b>	<b>0.2344</b>

with different values ( $\alpha=1.0, 1.4, 1.8, 2.2$ ) in Table XI. The results demonstrate a bell-shaped performance curve, where  $\alpha=1.8$  achieves optimal balance between molecular expression accuracy and histological structure preservation.

**TABLE XI:** ABLATION STUDY OF FOD  $\alpha$  ON MIST DATASET. THE BEST SCORES ARE HIGHLIGHTED IN BOLD.

FOD $\alpha$	Quality		Pathology		Perception	
	PSNR $\uparrow$	SSIM $\uparrow$	IOD $\times 10^7$	Pearson-R $\uparrow$	FID $\downarrow$	DISTS $\downarrow$
1.0	14.6189	0.2115	-2.2031	0.8331	43.8208	0.2395
1.4	<b>14.6242</b>	0.2078	-1.7750	0.8598	38.3692	0.2372
1.8	14.3421	0.2032	<b>-0.3223</b>	<b>0.8649</b>	<b>38.0654</b>	<b>0.2344</b>
2.2	14.2708	<b>0.2197</b>	-1.8733	0.8507	43.6559	0.2449

## V. DISCUSSION

### A. Pathology Foundation Models Influence

We evaluated several vision–language foundation models — PLIP, MUSK, and CONCH — by swapping the foundation model used for text-guided virtual staining. Both PLIP and MUSK yield reasonable results under our framework, demonstrating that the proposed text-guided virtual staining pipeline is generally stable across different foundation models. However, since PLIP and MUSK were not trained on large-scale immunohistochemistry (IHC) data, they fail to capture the domain-specific embeddings required for subtle biomarker distinctions among HER2, ER, PR, and Ki67. We excluded models such as UNI and Virchow because they provide only image encoders and lack text encoders, which are essential for our prompt-guided framework. In contrast, CONCH was pre-trained on large-scale IHC pathological images and thus encodes rich pathology-specific features that better support text-guided control over fine-grained tissue and biomarker structures. Consequently, when used as the foundation for text guidance, CONCH achieves the best feature-level consistency metrics (Table XII), highlighting the benefit of using a domain-specialized foundation model for reliable text-guided virtual staining.

**TABLE XII:** ABLATION STUDY OF PATHOLOGICAL GUIDANCE MECHANISM ON MIST DATASET. THE BEST SCORES ARE HIGHLIGHTED IN BOLD.

Guidance	Quality		Pathology		Perception	
	PSNR $\uparrow$	SSIM $\uparrow$	IOD $\times 10^7$	Pearson-R $\uparrow$	FID $\downarrow$	DISTS $\downarrow$
PLIP	14.2897	<b>0.2111</b>	+0.6578	0.8476	41.4264	0.2511
MUSK	<b>14.7346</b>	0.2089	-2.5387	0.8408	40.6992	0.2499
CONCH	14.3421	0.2032	<b>-0.3223</b>	<b>0.8649</b>	<b>38.0654</b>	<b>0.2344</b>

### B. Revisiting PSNR and SSIM as Evaluation Metrics for Virtual Staining

Specifically, in the virtual stain datasets (MIST and IHC4BC), the tissue samples for different stains originate from serial sections of the same specimen. Despite WSI-level registration, local tissue deformations and nonrigid morphological differences persist at the patch level. To further analyze the effect of image degradation, we simulate blurriness in the reference IHC images using Gaussian kernels of varying strengths. As observed by Zhu et al. [32], introducing additional blur on top of already blurry IHC images can paradoxically increase the evaluation scores of virtual staining models (e.g., higher PSNR and SSIM), while the corresponding scores computed between the blurred labels and the original reference continue to decrease. This phenomenon highlights that conventional pixel-level metrics may overestimate performance when the outputs become perceptually smoother but biologically less faithful.

To further illustrate this limitation, we evaluated PSNR and SSIM after applying Gaussian blur with different kernel sizes (Table XIII). Interestingly, increasing the blur level consistently improved both metrics, despite the apparent loss of fine structural details. This counterintuitive trend indicates that PSNR and SSIM are better suited as relative references rather than absolute indicators of perceptual or diagnostic quality in virtual staining tasks.

**TABLE XIII:** COMPARISON OF PSNR AND SSIM VALUES WITH DIFFERENT GAUSSIAN BLUR KERNELS

Method	PSNR				SSIM			
	No Blur	3 $\times$ 3	5 $\times$ 5	7 $\times$ 7	No Blur	3 $\times$ 3	5 $\times$ 5	7 $\times$ 7
CycleGAN	13.3060	13.4611	13.5518	13.6656	0.2000	0.2264	0.2401	0.2561
Pix2Pix	14.3445	14.4810	14.5597	14.6546	0.2143	0.2407	0.2558	0.2726
CUT	14.2183	14.3632	14.4553	14.5692	0.2047	0.2318	0.2466	0.2633
ASP	14.2746	14.4244	14.5189	14.6330	0.2144	0.2406	0.2553	0.2719
Pyramid	14.3320	14.4816	14.5731	14.6877	0.2137	0.2402	0.2554	0.2715
TDKStain	14.6360	14.7828	14.8702	14.9784	0.2181	0.2427	0.2563	0.2718
PSPStain	14.4773	14.6160	14.6973	14.8003	0.2206	0.2458	0.2605	0.2767
DDBM	14.2916	14.3597	14.4136	14.4891	0.2278	0.2412	0.2511	0.2644
UNSB	13.6369	13.6961	13.7460	13.8196	0.2467	0.2545	0.2610	0.2702
ControlNet	9.1163	9.1449	9.1639	9.1938	0.1890	0.1977	0.2039	0.2122
VIMs	13.7730	14.0284	14.1404	14.2622	0.1848	0.2238	0.2436	0.2648
UMDST	13.4638	13.5209	13.5664	13.6294	0.2455	0.2562	0.2638	0.2736
PGVMS	14.3421	14.5022	14.6046	14.7304	0.2032	0.2298	0.2453	0.2624
Label	-	36.4453	33.0669	30.3883	-	0.9627	0.9189	0.8530

### C. Training Efficiency and Scalability

PGVMS serves as a unified model for multiplex staining, maintaining a compact architecture with a model size of 26.35 MB and requiring 16,540 MB of GPU memory during training on 512 $\times$ 512 patches cropped from 1024 $\times$ 1024 whole-slide regions. The training process completes within 125 hours across four stain datasets for 80 epochs.

During inference, PGVMS achieves high throughput and scalability on whole-slide images (WSIs). For 1024 $\times$ 1024 tiles, the model processes each tile in 0.0208 seconds using 10,284 MB GPU memory.

These results (Table XIV) demonstrate that PGVMS is computationally efficient, has a low memory footprint, and

**TABLE XIV:** Computational efficiency of PGVMS during training and inference.

Stage	Input Size	GPU (MB)	Time
Training	512 × 512	16,540	125 h / 80 epochs
Inference	1024 × 1024	10,284	0.0208 s / tile

scales well for large WSIs, making it suitable for clinical virtual staining applications.

#### D. Prompt Robustness Evaluation of PGVMS

We evaluated PGVMS under diverse prompt formulations to assess its robustness to linguistic variability. For each biomarker (HER2, ER, PR, Ki67), six prompts were designed and categorized by length and semantic richness—ranging from concise functional descriptions (*short*, e.g., “H&E to HER2/ER/PR/Ki67 stain conversion”), to moderately descriptive expressions (*medium*, e.g., “Convert H&E histology slide to HER2/ER/PR/Ki67 staining”), and semantically enriched, context-aware formulations (*long*, e.g., “Convert this H&E WSI patch to a HER2/ER/PR/Ki67 stain, ensuring the highest possible fidelity and biological plausibility”). In addition, we included the *original* prompt (“From an H&E stained image transfer to a HER2/ER/PR/Ki67 stained image”) as a reference, consistent with the default training configuration.

Table XV reports the quantitative comparison under different prompt formulations. Following prior prompt-guided virtual staining studies such as VIMs [16], we analyze prompt robustness by categorizing prompts according to their length and semantic informativeness, reflecting increasing levels of linguistic and biological conditioning. Overall, PGVMS exhibits only minor and acceptable performance variations across short (~5 words), medium (~10 words), and long (~18 words) prompts, indicating that the model is not overly sensitive to prompt formulation.

**TABLE XV:** ROBUSTNESS EVALUATION OF PGVMS UNDER DIFFERENT PROMPT EXPRESSIONS. THE BEST SCORES ARE HIGHLIGHTED IN BOLD.

Length	Prompt	Quality		Pathology		Perception	
		PSNR $\uparrow$	SSIM $\uparrow$	IOD $\times 10^7$	Pearson-R $\uparrow$	FID $\downarrow$	DISTS $\downarrow$
Short	1	14.4628	0.2211	-0.9492	0.8284	44.6465	0.2420
	2	14.2855	0.2092	-0.5466	0.8433	38.4802	0.2385
Medium	3	14.2589	<b>0.2333</b>	-1.7759	0.7235	53.0694	0.2541
	4	14.4086	0.2160	-1.4156	0.8326	40.1634	0.2410
Long	5	14.4193	0.2245	-1.2309	0.7994	46.1909	0.2441
	6	<b>14.4716</b>	0.2300	-1.8585	0.7977	46.4370	0.2454
Origin	-	14.3421	0.2032	<b>-0.3223</b>	<b>0.8649</b>	<b>38.0654</b>	<b>0.2344</b>

Consistent with observations in VIMs [16], increasing prompt length or semantic richness does not necessarily translate into improved virtual staining quality, and may even introduce slight degradations in certain metrics. This suggests that overly complex descriptions can introduce redundant or noisy semantic cues. By leveraging the CONCH-guided embedding, PGVMS is able to extract domain-relevant semantic information from concise and moderately informative prompts without relying on overly verbose descriptions, thereby preserving biological plausibility across diverse prompt formulations.

#### E. Generalization to Unseen Clinical Breast Cancer Patients

To demonstrate the generalization ability of our method to unseen patients, we evaluated PGVMS on a private clinical breast cancer dataset. A small subset of this dataset (9 ROIs) contains all four IHC stains (HER2, ER, PR, Ki-67), with each image cropped from whole-slide images (WSIs) into patches of size 4096 × 3072.

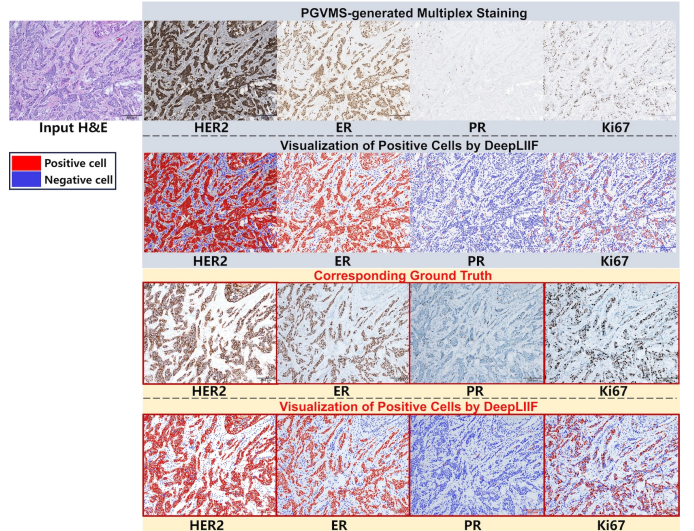


**Fig. 12:** Virtual IHC-stained image results on the clinical dataset, showing four stains (HER2, ER, PR, Ki-67) and positive cell visualization obtained using DeepLIF. The first column shows the input H&E images. Images with a gray background represent PGVMS-generated multiplex stains along with their corresponding positive cell visualization, while images with a yellow background show the ground truth multiplex stains and the associated positive cell visualization.

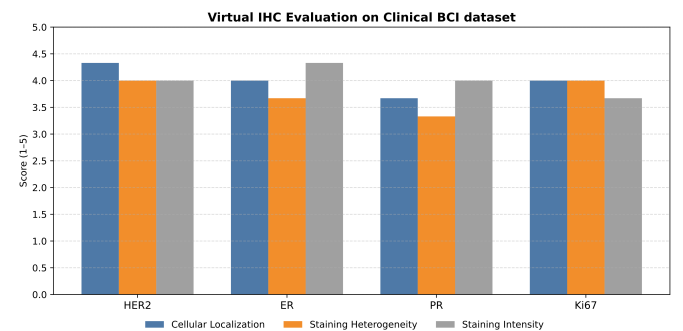


**Fig. 13:** Virtual IHC-stained image results on the clinical dataset. PGVMS preserves accurate cellular localization and realistic staining intensity across different biomarker.

As shown in Figure 12, our method robustly generates all four stains for previously unseen patients, demonstrating strong generalization at the patient level. An experienced pathologist evaluated the virtual IHC-stained images on a five-point scale (1–5) across three criteria: cellular localization, staining heterogeneity, and staining intensity, as shown in

Figure 13. These results indicate that PGVMS can effectively handle variations in tissue morphology and staining patterns, supporting its potential applicability in diverse clinical scenarios.

### F. Cross-Organ and Cross-Cancer Generalization of PGVMS

To evaluate the generalization ability of our PGVMS framework across different organs, cancer types, and IHC biomarkers, we conducted experiments on multiple independent clinical datasets, covering colon, liver, nasopharyngeal, and head-and-neck cancers. For each organ, we collect representative ROIs containing key biomarkers (e.g., Ki-67 for colorectal, HepPar1 for liver, EBER and CK for nasopharyngeal carcinoma, PD-L1 for head and neck).

1) *Clinical Colon Cancer Dataset*: We collected 69 ROIs from WSIs, each with paired upper and lower sections stained with H&E and Ki-67 IHC. ROIs were cropped to  $4096 \times 3072$  patches, and transfer learning for 10 epochs was applied.

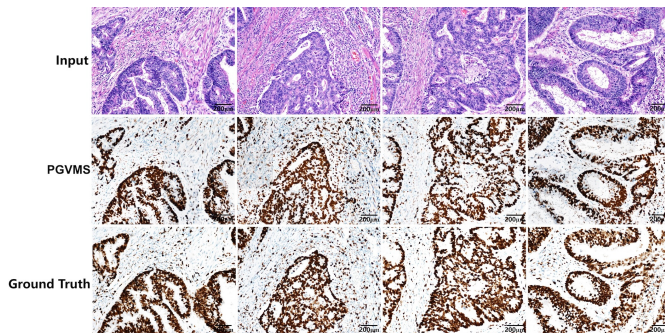


Fig. 14: Virtual Ki-67-stained image results on the clinical colon cancer dataset.

PGVMS synthesizes Ki-67-stained images (Fig. 14) with clear nuclear localization and structural fidelity comparable to the reference IHC slides.

2) *Clinical Hepatocellular Carcinoma (HCC) Dataset*: 38 ROIs with paired H&E and HepPar1 IHC sections were cropped to  $4096 \times 3072$ , and transfer learning was applied for 10 epochs.

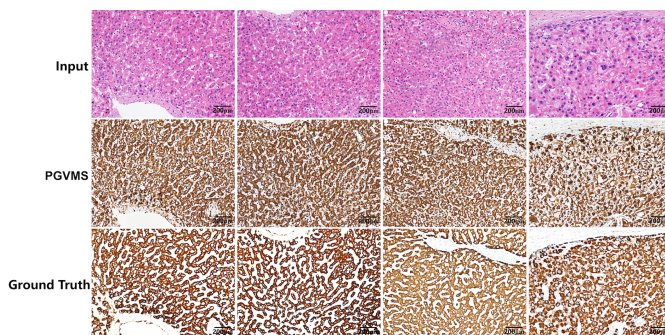


Fig. 15: Virtual HepPar1 IHC-stained image results on the clinical HCC dataset.

PGVMS (Fig. 15) preserves hepatocyte morphology and cytoplasmic staining patterns consistent with ground-truth slides.

3) *Clinical Nasopharyngeal Carcinoma (NPC) Dataset*: 57 ROIs were collected: 46 cases with CK and EBER stains, 11 cases with CK only. ROIs were cropped to  $4096 \times 3072$ , and the pretrained model was fine-tuned for 10 epochs.

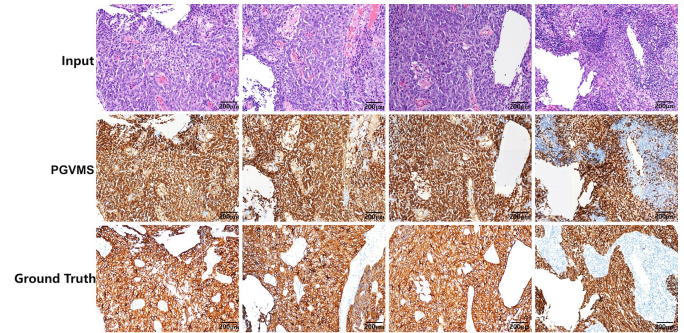


Fig. 16: Virtual CK-stained image results on the clinical NPC dataset.

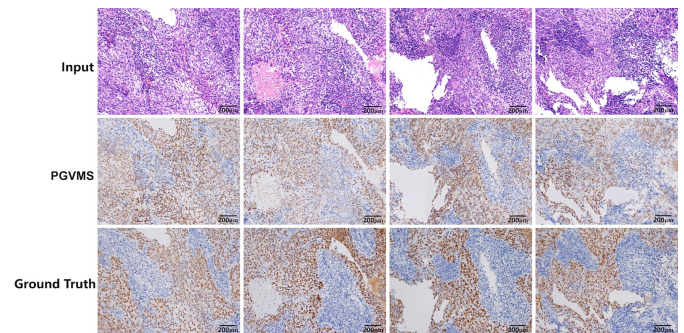


Fig. 17: Virtual EBER-stained image results on the clinical NPC dataset.

PGVMS synthesizes CK and EBER stains (Fig. 16 and Fig. 17) with realistic contrast and structural fidelity comparable to reference slides.

4) *Clinical Head and Neck Squamous Cell Carcinoma (HNSCC) Datasets*: 17 ROIs with paired H&E and PD-L1 IHC sections were cropped to  $4096 \times 3072$  patches, and the model was fine-tuned for 10 epochs.

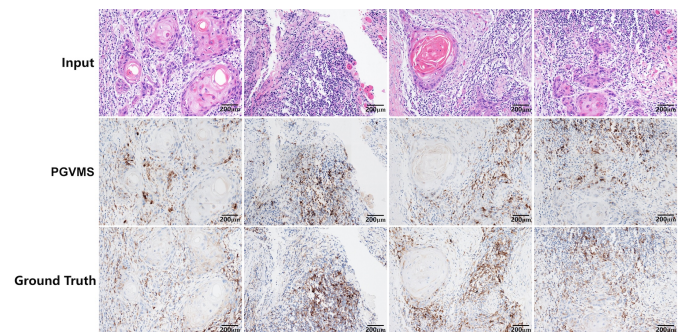


Fig. 18: Virtual PD-L1 IHC-stained image results on the clinical HNSCC dataset.

PGVMS generates virtual PD-L1-stained images (Fig. 18) exhibiting realistic membrane staining and expression intensity consistent with reference slides.

5) *Pathologist Evaluation*: Experienced pathologist was asked to evaluate the virtual IHC-stained images on a five-point scale (1–5) across three aspects: cellular localization, staining heterogeneity, and staining intensity in Fig. 19.

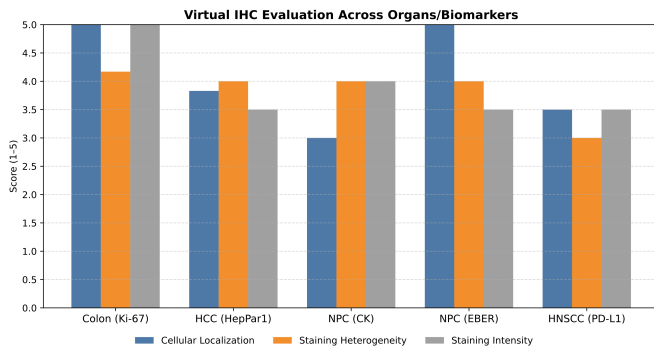


Fig. 19: Representative cross-organ virtual IHC staining results on liver, head-and-neck, colorectal, and nasopharyngeal samples. PGVMS preserves accurate cellular localization and realistic staining intensity across different biomarkers.

Specifically, Ki-67 and EBER achieve the highest overall ratings, demonstrating accurate nuclear localization and strong contrast between positive and negative regions. HepPar1 also performs well, showing clear cytoplasmic staining with minimal artefacts. PD-L1 and CK exhibit stable results across all three aspects, confirming the robustness of PGVMS on diverse tissue structures and staining patterns. Across all datasets, PGVMS demonstrates strong cross-organ and cross-cancer generalization, accurately synthesizing multiple IHC stains from H&E images, maintaining morphological fidelity, and preserving biologically meaningful staining patterns suitable for diverse clinical scenarios.

## VI. CONCLUSION

In this work, we present PGVMS, a comprehensive framework for pathological prompt-guided IHC virtual multiplex staining using only uniplex training data. Our three key innovations: (1) the pathological semantics-style guided (PSSG) generator with CONCH integration, (2) protein-aware learning strategy (PALS) with focal optical density mapping and (3) prototype-consistent learning strategy (PCLS) collectively address the critical challenges of semantic preservation, molecular-level accuracy, and spatial alignment in stain transformation. Extensive validation on MIST, IHC4BC, and cross-organ clinical datasets demonstrates state-of-the-art performance, with our method outperforming existing generative approaches while requiring no additional annotations. This work bridges a critical gap in computational pathology by evolving virtual staining from isolated single-task solutions to an integrated system supporting multiplex diagnosis via prompt-based control.

Our method, through the PCLS module, performs particularly well on clustered IHC patterns. However, biomarkers such as Ki-67, which display more dispersed staining, may be less optimally captured, whereas regions with contiguous positive cells are handled more effectively. Additionally, the

framework does not explicitly incorporate biomarker-specific spatial priors. For instance, HER2 is membrane-bound, ER/PR are nuclear, and Ki-67 labels proliferating nuclei. Incorporating such localization constraints could further enhance biological realism and produce virtual staining results that are more clinically plausible.

In future work, we plan to investigate strategies to better handle dispersed IHC staining patterns and to explore the scalability of PGVMS for multiplex IHC applications. By explicitly leveraging heterogeneous spatial information across different IHC stains, we aim to improve the biological realism, robustness, and clinical utility of virtual multiplex staining.

## REFERENCES

- [1] H. Irshad, “Automated mitosis detection in color and multi-spectral high-content images in histopathology: application to breast cancer grading in digital pathology,” Ph.D. dissertation, Université de Grenoble, 2014.
- [2] P. Weitz, M. Valkonen, L. Solorzano, C. Carr, K. Kartasalo, C. Boissin, S. Koivukoski, A. Kuusela, D. Rasic, Y. Feng *et al.*, “A multi-stain breast cancer histological whole-slide-image data set from routine diagnostics,” *Scientific Data*, vol. 10, no. 1, p. 562, 2023.
- [3] P. Harms, T. L. Frankel, M. Moutafi *et al.*, “Multiplex immunohistochemistry and immunofluorescence: a practical update for pathologists,” *Modern Pathology*, vol. 36, no. 7, p. 100197, 2023.
- [4] P. Isola, J.-Y. Zhu, T. Zhou, and A. A. Efros, “Image-to-image translation with conditional adversarial networks,” in *Proceedings of the IEEE/CVF Conference on Computer Vision and Pattern Recognition*, 2017, pp. 1125–1134.
- [5] T. Park, A. A. Efros, R. Zhang, and J.-Y. Zhu, “Contrastive learning for unpaired image-to-image translation,” in *European conference on computer vision*. Springer, 2020, pp. 319–345.
- [6] J.-Y. Zhu, T. Park, P. Isola, and A. A. Efros, “Unpaired image-to-image translation using cycle-consistent adversarial networks,” in *Proceedings of the IEEE/CVF International Conference on Computer Vision*, 2017, pp. 2223–2232.
- [7] B. Zeng, Y. Lin, Y. Wang, Y. Chen, J. Dong, X. Li, and Y. Zhang, “Semi-supervised pr virtual staining for breast histopathological images,” in *Medical Image Computing and Computer Assisted Intervention – MICCAI 2022: 25th International Conference, Singapore, September 18–22, 2022, Proceedings, Part II*. Springer, 2022, pp. 232–241.
- [8] S. Liu, C. Zhu, F. Xu, X. Jia, Z. Shi, and M. Jin, “Bci: Breast cancer immunohistochemical image generation through pyramid pix2pix,” in *Proceedings of the IEEE/CVF Conference on Computer Vision and Pattern Recognition*, 2022, pp. 1815–1824.
- [9] R. Zhang, Y. Cao, Y. Li, Z. Liu, J. Wang, J. He, C. Zhang, X. Sui, P. Zhang, L. Cui *et al.*, “Mvfstain: multiple virtual functional stain histopathology images generation based on specific domain mapping,” *Medical Image Analysis*, vol. 80, p. 102520, 2022.
- [10] F. Li, Z. Hu, W. Chen, and A. Kak, “Adaptive supervised patchnce loss for learning h&e-to-ihc stain translation with inconsistent groundtruth image pairs,” in *Medical Image Computing and Computer Assisted Intervention – MICCAI 2023: 26th International Conference, Vancouver, BC, Canada, October 8–12, 2023, Proceedings, Part VI*. Springer, 2023, pp. 632–641.
- [11] S. Liu, B. Zhang, Y. Liu, A. Han, H. Shi, T. Guan, and Y. He, “Unpaired stain transfer using pathology-consistent constrained generative adversarial networks,” *IEEE Transactions on Medical Imaging*, vol. 40, no. 8, pp. 1977–1989, 2021.
- [12] Q. Peng, W. Lin, Y. Hu, A. Bao, C. Lian, W. Wei, M. Yue, J. Liu, L. Yu, and L. Wang, “Advancing h&e-to-ihc virtual staining with task-specific domain knowledge for her2 scoring,” in *International Conference on Medical Image Computing and Computer-Assisted Intervention*. Springer, 2024, pp. 3–13.
- [13] F. Chen, R. Zhang, B. Zheng, Y. Sun, J. He, and W. Qin, “Pathological semantics-preserving learning for h&e-to-ihc virtual staining,” in *International Conference on Medical Image Computing and Computer-Assisted Intervention*. Springer, 2024, pp. 384–394.
- [14] X. Guan, Z. Zhang, Y. Wang, Y. Zhang, D. Jiang, and Y. Zhang, “Correlated multiple ihc virtual staining for breast histopathological images,” in *ICASSP 2025-2025 IEEE International Conference on Acoustics, Speech and Signal Processing (ICASSP)*. IEEE, 2025, pp. 1–5.

- [15] Y. Lin, B. Zeng, Y. Wang, Y. Chen, Z. Fang, J. Zhang, X. Ji, H. Wang, and Y. Zhang, "Unpaired multi-domain stain transfer for kidney histopathological images," in *Proceedings of the AAAI Conference on Artificial Intelligence*, vol. 36, no. 2, 2022, pp. 1630–1637.
- [16] S. Dubey, Y. Chong, B. Knudsen, and S. Y. Elhabian, "Vims: virtual immunohistochemistry multiplex staining via text-to-stain diffusion trained on uniplex stains," in *International Workshop on Machine Learning in Medical Imaging*. Springer, 2024, pp. 143–155.
- [17] H. Kazemi, S. Soleymani, F. Taherkhani, S. Iranmanesh, and N. Nasrabadi, "Unsupervised image-to-image translation using domain-specific variational information bound," *Advances in neural information processing systems*, vol. 31, 2018.
- [18] A. CycleGAN, "Learning many-to-many mappings from unpaired data," *Amjad Almahairi, Sai Rajeswa, Alessandro Sordoni, Philip Bachman, Aaron Courville*, 2018.
- [19] L. Zhang, A. Rao, and M. Agrawala, "Adding conditional control to text-to-image diffusion models," in *Proceedings of the IEEE/CVF international conference on computer vision*, 2023, pp. 3836–3847.
- [20] B. Kim, G. Kwon, K. Kim, and J. C. Ye, "Unpaired image-to-image translation via neural Schrödinger bridge," *arXiv preprint arXiv:2305.15086*, 2023.
- [21] L. Zhou, A. Lou, S. Khanna, and S. Ermon, "Denoising diffusion bridge models," *arXiv preprint arXiv:2309.16948*, 2023.
- [22] B. Xiong, Y. Peng, R. Zhang, F. Chen, J. He, and W. Qin, "Unpaired multi-domain histopathology virtual staining using dual path prompted inversion," in *Proceedings of the AAAI Conference on Artificial Intelligence*, vol. 39, no. 8, 2025, pp. 8780–8787.
- [23] A. Radford, J. W. Kim, C. Hallacy, A. Ramesh, G. Goh, S. Agarwal, G. Sastry, A. Askell, P. Mishkin, J. Clark *et al.*, "Learning transferable visual models from natural language supervision," in *International conference on machine learning*. PmlR, 2021, pp. 8748–8763.
- [24] J. Xiang, X. Wang, X. Zhang, Y. Xi, F. Eweje, Y. Chen, Y. Li, C. Bergstrom, M. Gopaulchan, T. Kim *et al.*, "A vision–language foundation model for precision oncology," *Nature*, vol. 638, no. 8051, pp. 769–778, 2025.
- [25] Z. Huang, F. Bianchi, M. Yuksekogonul, T. J. Montine, and J. Zou, "A visual–language foundation model for pathology image analysis using medical twitter," *Nature medicine*, vol. 29, no. 9, pp. 2307–2316, 2023.
- [26] M. Y. Lu, B. Chen, D. F. Williamson, R. J. Chen, I. Liang, T. Ding, G. Jaume, I. Odintsov, L. P. Le, G. Gerber *et al.*, "A visual-language foundation model for computational pathology," *Nature Medicine*, vol. 30, no. 3, pp. 863–874, 2024.
- [27] F. Varghese, A. B. Bukhari, R. Malhotra, and A. De, "Ihc profiler: an open source plugin for the quantitative evaluation and automated scoring of immunohistochemistry images of human tissue samples," *PloS one*, vol. 9, no. 5, p. e96801, 2014.
- [28] A. v. d. Oord, Y. Li, and O. Vinyals, "Representation learning with contrastive predictive coding," *arXiv preprint arXiv:1807.03748*, 2018.
- [29] A. Akbarnejad, N. Ray, P. J. Barnes *et al.*, "Predicting ki67, er, pr, and her2 statuses from h&e-stained breast cancer images," *arXiv preprint arXiv:2308.01982*, 2023, preprint.
- [30] P. Ghahremani, Y. Li, A. Kaufman, R. Vanguri, N. Greenwald, M. Angelo, T. J. Hollmann, and S. Nadeem, "Deep learning-inferred multiplex immunofluorescence for immunohistochemical image quantification," *Nature machine intelligence*, vol. 4, no. 4, pp. 401–412, 2022.
- [31] Z.-C. Li, W. Qin, D. Liang, and H. Zheng, "Biomedical ai: Evolving from digital to physical and biological intelligence," *The Innovation Informatics*, vol. 1, no. 1, pp. 100 010–1, 2025.
- [32] C. Zhu, S. Liu, Z. Yu, F. Xu, A. Aggarwal, G. Corredor, A. Madabhushi, Q. Qu, H. Fan, F. Li *et al.*, "Breast cancer immunohistochemical image generation: a benchmark dataset and challenge review," *arXiv preprint arXiv:2305.03546*, 2023.